

Reliable methods for seamless stitching of tight-binding models based on maximally localized Wannier functions

Jae-Mo Lihm¹ and Cheol-Hwan Park^{1,*}

¹*Department of Physics, Seoul National University, Seoul 08826, Korea*
(Dated: March 12, 2022)

Maximally localized Wannier functions are localized orthogonal functions that can accurately represent given Bloch eigenstates of a periodic system at a low computational cost, thanks to the small size of each orbital. Tight-binding models based on the maximally localized Wannier functions obtained from different systems are often combined to construct tight-binding models for large systems such as a semi-infinite surface. However, the corresponding maximally localized Wannier functions in the overlapping region of different systems are not identical, and this discrepancy can introduce serious artifacts to the combined tight-binding model. Here, we propose two methods to seamlessly stitch two different tight-binding models that share some basis functions in common. First, we introduce a simple and efficient method: (i) finding the best matching maximally localized Wannier function pairs in the overlapping region belonging to the two tight-binding models, (ii) rotating the spin orientations of the two corresponding Wannier functions to make them parallel to each other, and (iii) making their overall phases equal. Second, we propose a more accurate and generally applicable method based on the iterative minimization of the difference between the Hamiltonian matrix elements in the overlapping region. We demonstrate our methods by applying them to the surfaces of diamond, GeTe, Bi₂Se₃, and TaAs. Our methods can be readily used to construct reliable tight-binding models for surfaces, interfaces, and defects.

I. INTRODUCTION

In the independent-particle approximation, eigenstates of a periodic electronic system are given by Bloch states $|\psi_{p\mathbf{k}}\rangle$, labelled with the band index p and the reciprocal vector index \mathbf{k} . Wannier functions (WFs) are an alternative representation of the Bloch states that provide an atomic-orbital-like, localized basis set. The WFs are obtained by first performing a unitary transformation to generate N_W Bloch states at each \mathbf{k} point

$$|\tilde{\psi}_{n\mathbf{k}}\rangle = \sum_p |\psi_{p\mathbf{k}}\rangle U_{pn}(\mathbf{k}) \quad (1)$$

and then Fourier transforming the periodic Bloch states into localized WFs:

$$|w_{\mathbf{R}n}\rangle = \frac{V_{\text{cell}}}{(2\pi)^3} \int_{\text{BZ}} d\mathbf{k} e^{-i\mathbf{k}\cdot\mathbf{R}} |\tilde{\psi}_{n\mathbf{k}}\rangle. \quad (2)$$

Here, N_W is also the number of Wannier functions per unit cell, V_{cell} is the volume of the real-space unit cell, and the integration is performed over the Brillouin zone (BZ). Also, the WFs are labelled by the orbital index n and the unit cell index \mathbf{R} . In actual calculations, the Brillouin zone is sampled with a uniform \mathbf{k} -point mesh. In this case, the WFs become

$$|w_{\mathbf{R}n}\rangle = \frac{1}{\sqrt{N_k}} \sum_{\mathbf{k}} \sum_p e^{-i\mathbf{k}\cdot\mathbf{R}} |\psi_{p\mathbf{k}}\rangle U_{pn}^{\mathbf{k}}, \quad (3)$$

where N_k is the number of \mathbf{k} points in the mesh.

Given a set of Bloch states, the corresponding set of WFs is not unique. This degree of freedom is parameterized by the unitary matrix $U^{\mathbf{k}}$ defined at each \mathbf{k} point of the mesh. A commonly used method to determine the

$U^{\mathbf{k}}$ matrices is to choose them such that the resulting WFs are as localized as possible in real space. The WFs that minimize the total spread functional

$$\Omega = \sum_{n=1}^{N_W} \left[\langle w_{0n} | r^2 | w_{0n} \rangle - \langle w_{0n} | \mathbf{r} | w_{0n} \rangle^2 \right] \quad (4)$$

are termed maximally localized Wannier functions (MLWFs)¹⁻³. Since the MLWFs are maximally localized in real space, they are often used to generate an accurate and transferable tight-binding model of an electronic system with the smallest possible set of hopping integrals³. This tight-binding model correctly reproduces the band structure obtained by the *ab initio* calculation that the MLWFs are calculated from. Thus, this model is called an *ab initio* tight-binding model based on MLWFs³.

Furthermore, one can combine the *ab initio* tight-binding models based on MLWFs obtained from different systems to construct a tight-binding model for a large-scale system. For example, the tight-binding models for the bulk and a small supercell of a given material can be combined to describe disordered systems⁴, impurities⁵, interfaces⁶⁻⁸, and surfaces⁹⁻¹².

Among these composite systems, we focus on the modelling of surfaces. The electronic structure of a surface can be modelled by constructing a tight-binding model of a finite slab or a semi-infinite surface where the hopping parameters are obtained from the *ab initio* tight-binding model based on the WFs of the *bulk* crystal¹⁰⁻¹². The bulk-derived surface model correctly reproduces the topological properties of the bulk such as the presence or absence of topologically protected surface states. However, this model cannot take the difference in the environment of the surface from the bulk, surface charge redistribution, and structural relaxation into account. Hence,

the calculated properties of the bulk-derived surface may significantly differ from the those of the real surface¹³.

A more accurate method to describe surfaces is to construct a tight-binding model of a semi-infinite surface by combining the MLWF-based tight-binding models for the bulk and a thin slab of a given material⁹ as illustrated in Fig. 1. This construction is done by dividing the system into principal layers¹⁴. A principal layer is a group of atomic layers which is sufficiently thick such that the hopping between different principal layers is negligible except between the nearest neighbors. To combine the MLWF-based tight-binding models, first, we regard the principal layer at the center of the thin slab as a bulk principal layer. Note that the *thin* slab should be *thick* enough such that the hopping integrals in the principal layer in the middle of the slab converge to those in the corresponding principal layer in the true bulk system. Then, the bottom-surface principal layer is removed so that the slab has only the top-surface principal layer and one bulk principal layer. Now, at the bottom of this composite system, we append an infinite number of bulk principal layers to make a semi-infinite surface. The constructed tight-binding model for the semi-infinite surface can take the surface-local changes of the hopping parameters into account. This scheme can be straightforwardly modified to model a thick but finite slab by inserting a finite number of bulk principal layers between the top- and bottom-surface principal layers of the thin slab. The electronic structure of the combined semi-infinite surface and the finite slab can be calculated by iterative calculation of the surface Green function¹⁵ and by direct diagonalization, respectively.

When the tight-binding models of the bulk and slab based on MLWFs are combined, the difference between the MLWFs of the two systems should be taken care of. Due to the maximal localization procedure, the MLWFs in the bulk and those in the center of the slab could be different from each other even if the local atomic structure and the initial guess functions are the same. Several factors can contribute to this discrepancy. First, MLWFs can be arbitrarily permuted among themselves and be multiplied by overall phases because these operations do not change the total spread. Also, for calculations with spin-orbit coupling (SOC), the corresponding MLWFs of the bulk and the slab can have different spin orientations. Finally, the orbital part of the MLWFs obtained from the bulk and the slab can have nontrivial differences. If these discrepancies are not properly handled, they can act as non-physical impurities at the interface where the bulk and the slab tight-binding models are combined. These impurities can lead to artifacts in the calculated physical quantities. Therefore, it is important to correct the differences between the MLWFs before combining the tight-binding models. Throughout this paper, we call that the bulk and slab tight-binding models based on MLWFs are “seamlessly stitched” if the difference between the corresponding bulk and slab MLWFs is made small.

In this paper, we propose two post-processing meth-

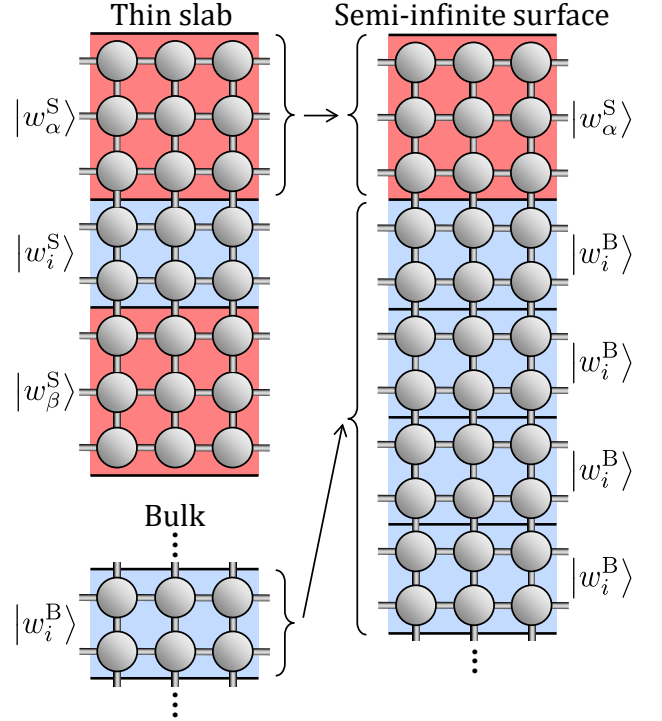


FIG. 1. Schematic illustration of the construction of the tight-binding model for a semi-infinite surface from the tight-binding models of a bulk and a thin slab. The principal layers are indicated by shaded areas separated by horizontal solid black lines. The regions with red (dark gray) background correspond to the surface principal layers, in which the surface-local perturbations to the on-site energies and hopping parameters are present. The regions with blue (light gray) background are bulk principal layers, where these surface-local perturbations are negligible. A grey sphere represent each atomic site hosting MLWFs. The ket vectors of the MLWFs are written alongside the principal layers where the MLWFs are located. The superscripts B and S indicate that the corresponding MLWFs are the basis functions of the tight-binding models of the bulk and the slab, respectively. Indices α and β are used to denote the MLWFs in the surface principal layers, while index i is used to denote the MLWFs in the bulk principal layer. The in-plane unit cell index \mathbf{R} is omitted for clarity. The system is assumed to be periodic in the in-plane directions although our method does not require in-plane periodicity.

ods to achieve seamless stitching of tight-binding models based on MLWFs. The first method is a simple and efficient correction: (i) find the best matching MLWF pairs in the overlapping principal layer of the bulk and slab tight-binding models, (ii) rotate the spin axes of the slab MLWFs to make them parallel to those of the corresponding bulk MLWFs, and (iii) make their overall phases equal. The second method is based on the minimization of the difference of the on-site and hopping parameters between the bulk and the slab tight-binding models and is more accurate and generally applicable.

The remainder of this paper is organized as follows.

In Sec. II, we describe the methods proposed in this paper in detail. We then illustrate the utility of our methods by applying them to the surfaces of diamond, GeTe, Bi₂Se₃, and TaAs. We specify the computational details in Sec. III, and present and discuss the results in Sec. IV. Another method often used to combine *ab initio* tight-binding models is to use the WFs obtained without maximal localization as the basis functions^{4,5,10}. These “projection-only” WFs are obtained by projecting the atomic-orbital-like initial guesses for the WFs onto the target subspace of Kohn-Sham eigenstates. We compare the projection-only WF method with the corrections proposed in this paper in Sec. V. Finally, we present a summary and conclude in Sec. VI.

II. METHODS

In this section, we explain our correction methods in detail. We focus on the seamless stitching of the bulk and the slab tight-binding models for constructing a tight-binding model of the surface. Hence, we describe the corrections that minimize the difference between the MLWFs at the interior of the slab and the corresponding MLWFs of the bulk system of the same material. However, the methods described in this section can be straightforwardly extended to other problems such as modelling of interfaces or impurities.

A. Correction on the Wannier functions

Let $|w_{\mathbf{R}i}^B\rangle$ and $|w_{\mathbf{R}n}^S\rangle$ denote the bulk and slab MLWFs, respectively. Here, the index \mathbf{R} denotes the bulk and slab lattice vectors *along the in-plane direction*, which is orthogonal to the surface normal direction of the slab. Indices $i \in \{1, 2, \dots, N_W^B\}$ and $n \in \{1, 2, \dots, N_W^S\}$, are the orbital indices, where N_W^B is the number of MLWFs per in-plane unit cell of the bulk principal layer and N_W^S is the number of MLWFs in the entire slab per in-plane unit cell. Since the slab is thicker than the bulk principal layer along the out-of-plane direction of the slab, there are more MLWFs per unit cell in the slab than in the bulk, i.e., $N_W^S > N_W^B$.

Within this setup, our task is to find the optimal linear transformation on $|w_{\mathbf{R}n}^S\rangle$'s to make new slab WFs, which we denote as $|\tilde{w}_{\mathbf{R}n}^S\rangle$, be as close as possible to $|w_{\mathbf{R}i}^B\rangle$ for $n = i$. In other words, we want to make

$$|\tilde{w}_{\mathbf{R}i}^S\rangle \approx |w_{\mathbf{R}i}^B\rangle \quad (5)$$

for $1 \leq i \leq N_W^B$. Here, the new slab WFs $|\tilde{w}_{\mathbf{R}i}^S\rangle$ are the WFs in the principal layer at the center of the slab. The similarity between the bulk WFs and the slab WFs in the center of the slab directly results in the seamless stitching of the bulk and the slab WFs because the WFs in the top and bottom surfaces of the slab are already seamlessly stitched with the WFs in the center of the slab by the construction of WFs.

In general, a linear transformation between the original and the new slab WFs is parameterized by a single $N_W^S N_k^S \times N_W^S$ matrix V :

$$|\tilde{w}_{\mathbf{R}'n}^S\rangle = \sum_{\mathbf{R}m} |w_{\mathbf{R}+\mathbf{R}'m}^S\rangle V_{\mathbf{R}m,0n}, \quad (6)$$

where we have used $V_{\mathbf{R}+\mathbf{R}'m,\mathbf{R}'n} = V_{\mathbf{R}m,0n}$. Here, N_k^S is the number of \mathbf{k} points in the Monkhorst-Pack mesh of the slab. Using Fourier transformation, one can decompose V into a sum of N_W^S dimensional square matrices defined at each \mathbf{k} point:

$$V_{\mathbf{R}m,0n} = \frac{1}{N_k^S} \sum_{\mathbf{k}} e^{i\mathbf{k}\cdot\mathbf{R}} V_{mn}^{\mathbf{k}}, \quad (7)$$

or, equivalently,

$$V_{mn}^{\mathbf{k}} = \sum_{\mathbf{R}} e^{-i\mathbf{k}\cdot\mathbf{R}} V_{\mathbf{R}m,0n}. \quad (8)$$

Since the constructed slab WFs must also form an orthonormal set, namely

$$\langle \tilde{w}_{\mathbf{R}m}^S | \tilde{w}_{\mathbf{0}n}^S \rangle = \delta_{\mathbf{R}m,0n}, \quad (9)$$

V should satisfy the constraint

$$\sum_{\mathbf{R}',m'} V_{\mathbf{R}m,\mathbf{R}'m'}^\dagger V_{\mathbf{R}'m',0n} = \delta_{\mathbf{R}m,0n}. \quad (10)$$

This is equivalent to the unitarity of each $V^{\mathbf{k}}$ matrix

$$V^{\mathbf{k}} V^{\mathbf{k}\dagger} = V^{\mathbf{k}\dagger} V^{\mathbf{k}} = I_S, \quad (11)$$

where I_S is the N_W^S dimensional square identity matrix. We note that the V matrix transforms the WFs within the Wannier subspace without altering the subspace itself.

Now, we define two criteria to evaluate the quality of the constructed WFs. The first criterion is based on the orthonormality of the WFs. If all of the new slab WFs are almost identical to the bulk MLWFs with the same orbital index, the orthonormality relation

$$\langle \tilde{w}_{\mathbf{R}n}^S | w_{\mathbf{0}i}^B \rangle \approx \delta_{n,i} \delta_{\mathbf{R},0} \quad (12)$$

would be satisfied; hence, we may use the deviation from Eq. (12) in measuring the resemblance between the two sets of WFs. We call the absolute deviation of the overlap between the bulk WF, $|w_{\mathbf{0}i}^B\rangle$, and the surface WF, $|\tilde{w}_{\mathbf{R}n}^S\rangle$, from orthonormality as the “individual overlap error” $|\Delta S_{\mathbf{R}n,0i}|$:

$$|\Delta S_{\mathbf{R}n,0i}| = |\langle \tilde{w}_{\mathbf{R}n}^S | w_{\mathbf{0}i}^B \rangle - \delta_{n,i} \delta_{\mathbf{R},0}|. \quad (13)$$

We also define the “average overlap error” ΔS_{ave} :

$$\Delta S_{\text{ave}} = \sqrt{\frac{1}{N_W^B} \sum_{i=1}^{N_W^B} \left(\sum_{\mathbf{R}} \sum_{n=1}^{N_W^S} |\Delta S_{\mathbf{R}n,0i}|^2 \right)}. \quad (14)$$

Note that ΔS_{ave} is bounded above by 2 in case $\langle \tilde{w}_{\mathbf{R}n}^S | w_{\mathbf{0}i}^B \rangle = -\delta_{n,i} \delta_{\mathbf{R},\mathbf{0}}$ for all \mathbf{R} , n , and i .

To derive the relation between the overlap error and the V matrix, we first define the overlap matrix A as the inner product of the bulk and slab MLWFs:

$$A_{\mathbf{R}m,0i} = \langle w_{\mathbf{R}m}^S | w_{\mathbf{0}i}^B \rangle. \quad (15)$$

Its Fourier transformation is

$$A_{mi}^{\mathbf{k}} = \sum_{\mathbf{R}} e^{-i\mathbf{k} \cdot \mathbf{R}} A_{\mathbf{R}m,0i}, \quad (16)$$

and, equivalently,

$$A_{\mathbf{R}m,0i} = \frac{1}{N_{\mathbf{k}}^S} \sum_{\mathbf{k}} e^{i\mathbf{k} \cdot \mathbf{R}} A_{mi}^{\mathbf{k}}. \quad (17)$$

The detailed procedures for obtaining A using first-principles density-functional theory (DFT) methods and plane-wave basis sets are described in Appendix A.

Given the A matrix, it is straightforward to calculate the overlap error therefrom. Using Eqs. (6), (7), (15), and (17), or the convolution property of Fourier transformation, one obtains

$$\begin{aligned} \langle \tilde{w}_{\mathbf{R}n}^S | w_{\mathbf{0}i}^B \rangle &= \sum_{\mathbf{R}',m} V_{\mathbf{R}n,\mathbf{R}'m}^\dagger \langle w_{\mathbf{R}'m}^S | w_{\mathbf{0}i}^B \rangle \\ &= \frac{1}{N_{\mathbf{k}}^S} \sum_{\mathbf{k}} e^{i\mathbf{k} \cdot \mathbf{R}} (V^{\mathbf{k}\dagger} A^{\mathbf{k}})_{ni}. \end{aligned} \quad (18)$$

Then, the individual overlap error is

$$\begin{aligned} |\Delta S_{\mathbf{R}n,0i}| &= \left| \frac{1}{N_{\mathbf{k}}^S} \sum_{\mathbf{k}} e^{i\mathbf{k} \cdot \mathbf{R}} (V^{\mathbf{k}\dagger} A^{\mathbf{k}})_{ni} - \delta_{n,i} \delta_{\mathbf{R},\mathbf{0}} \right| \\ &= \frac{1}{N_{\mathbf{k}}^S} \left| \sum_{\mathbf{k}} e^{i\mathbf{k} \cdot \mathbf{R}} (V^{\mathbf{k}\dagger} A^{\mathbf{k}} - I_{\text{SB}})_{ni} \right|, \end{aligned} \quad (19)$$

where $(I_{\text{SB}})_{ni} = \delta_{n,i}$. A simple expression for the average overlap error is obtained using Parseval's theorem:

$$\Delta S_{\text{ave}} = \sqrt{\frac{1}{N_{\mathbf{W}}^B N_{\mathbf{k}}^S} \sum_{\mathbf{k}} \|V^{\mathbf{k}\dagger} A^{\mathbf{k}} - I_{\text{SB}}\|_{\text{F}}^2}. \quad (20)$$

Here, $\|X\|_{\text{F}} = \sqrt{\text{Tr}(XX^\dagger)}$ is the Frobenius norm.

The overlap error is a direct measure of the quality of the corrected WFs. However, calculation of the overlap error can be troublesome, mainly because of the need to calculate the overlap matrix A . The matrix elements of A are the inner products between the bulk and the slab MLWFs. These values are not calculated in usual Wannierization procedures where the bulk and the slab MLWFs are computed separately. In addition, in plane-wave DFT calculations, the real-space values of the WFs are calculated on a discrete grid. The spacing of this grid is determined by the lattice constants and the wavefunction energy cutoff. If the out-of-plane lattice constants

of the bulk and the slab are incommensurate, the real-space grids also become incommensurate. It follows that the WFs need to be interpolated to calculate the overlap matrix A .

Moreover, when ultrasoft pseudopotential (USPP) or projector augmented wave (PAW) potential is used for the DFT calculation, the simple orthogonality condition between the bulk and the slab WFs [Eq. (12)] does not hold because only a generalized orthogonality relation between the pseudo wavefunctions is satisfied in such calculations^{16–18}. The generalized orthogonality relation is determined from the projector functions of the USPP or PAW potentials. In usual electronic structure calculations, the inner product between pseudo wavefunctions that belong to a single system can be calculated with the help of the generalized overlap matrix, also defined by the pseudopotential. However, since the bulk and the slab have different atomic positions, they have different sets of projector functions. Thus, one cannot use the generalized overlap matrix to recover orthogonality between the bulk and slab pseudo wavefunctions. Instead, the all-electron wavefunction should be restored, requiring a considerable computational effort.

In this paper, we circumvent these difficulties by using norm-conserving pseudopotentials and tuning the vacuum thickness to make the slab supercell commensurate with the bulk unit cell. But in general, it would be difficult to assess the quality of the constructed WFs using the overlap error.

Because of this difficulty, here we define the second criterion, which makes use of the Hamiltonian matrix elements of the tight-binding model. To combine the bulk and the slab tight-binding models, one has to make sure that the slab is thick enough so that the charge density around the center of the slab is nearly identical to that of the bulk. Then, the Hamiltonian at the center of the slab and the Hamiltonian of the bulk will be approximately the same. Therefore, the difference between the Hamiltonian matrix elements of the bulk and the slab can be attributed solely to the difference in the basis functions of the tight-binding models, which are the bulk and slab WFs. This second criterion does not require computation of quantities other than the Hamiltonian matrix elements, which are calculated in standard Wannierization procedures; hence, it can be readily used in actual calculations.

To be concrete, we define the individual hopping error

$$|\Delta H_{\mathbf{R}i,0j}| = |\langle \tilde{w}_{\mathbf{R}i}^S | H_{\text{S}} | \tilde{w}_{\mathbf{0}j}^S \rangle - \langle w_{\mathbf{R}i}^B | H_{\text{B}} | w_{\mathbf{0}j}^B \rangle| \quad (21)$$

and the average hopping error

$$\Delta H_{\text{ave}} = \sqrt{\frac{1}{N_{\mathbf{W}}^B} \sum_{j=1}^{N_{\mathbf{W}}^B} \left(\sum_{\mathbf{R}} \sum_{i=1}^{N_{\mathbf{W}}^B} |\Delta H_{\mathbf{R}i,0j}|^2 \right)} \quad (22)$$

analogously to the definition of the individual and average overlap errors in Eqs. (13) and (14). Here, H_{S} and H_{B} are the Hamiltonian operators for the bulk and the

slab, respectively. Note that only the hopping between the WFs in the central principal layer of the slab is taken into account, i.e., $i, j \in \{1, 2, \dots, N_W^B\}$.

Before calculating the hopping errors, the reference potential of the bulk and the slab calculation need to be aligned. We use the on-site energies of the MLWFs to determine the reference potential¹⁹. The difference in the average on-site energy

$$\delta H_{\text{on}} = \frac{1}{N_W^B} \sum_{i=1}^{N_W^B} (\langle w_{0i}^S | H_S | w_{0i}^S \rangle - \langle w_{0i}^B | H_B | w_{0i}^B \rangle) \quad (23)$$

is subtracted from all the on-site energies of the slab tight-binding model. Note that the reference potential of the slab is calculated using only the MLWFs at the central principal layer.

Once the average on-site potential energy of the slab tight-binding model is aligned with that of the bulk tight-binding model, the individual hopping errors associated with the given V matrix can be calculated from the MLWF hopping matrix elements using the convolution property, similarly as in Eq. (19):

$$\begin{aligned} |\Delta H_{\mathbf{R}i,0j}| &= \sum_{\mathbf{R}', \mathbf{R}'', m, n} V_{\mathbf{R}i, \mathbf{R}'m}^\dagger \langle w_{\mathbf{R}'m}^S | H_S | w_{\mathbf{R}''n}^S \rangle V_{\mathbf{R}''n, 0j} \\ &\quad - \langle w_{\mathbf{R}i}^B | H_B | w_{0j}^B \rangle \\ &= \frac{1}{N_k^S} \sum_{\mathbf{k}} e^{i\mathbf{k} \cdot \mathbf{R}} (V^{\mathbf{k}\dagger} H_S^{\mathbf{k}} V^{\mathbf{k}} - H_B^{\mathbf{k}})_{ij}. \end{aligned} \quad (24)$$

Here, we defined

$$(H_S^{\mathbf{k}})_{mn} = \sum_{\mathbf{R}} e^{-i\mathbf{k} \cdot \mathbf{R}} \langle w_{\mathbf{R}m}^S | H_S | w_{\mathbf{R}n}^S \rangle \quad (25)$$

and

$$(H_B^{\mathbf{k}})_{ij} = \sum_{\mathbf{R}} e^{-i\mathbf{k} \cdot \mathbf{R}} \langle w_{\mathbf{R}i}^B | H_B | w_{\mathbf{R}j}^B \rangle. \quad (26)$$

The sum over \mathbf{R} is calculated only over the in-plane lattice vectors.

The average hopping error can be calculated using Parseval's theorem:

$$\Delta H_{\text{ave}} = \sqrt{\frac{1}{N_W^B N_k^S} \sum_{\mathbf{k}} \left\| I_{\text{SB}}^\dagger V^{\mathbf{k}\dagger} H_S^{\mathbf{k}} V^{\mathbf{k}} I_{\text{SB}} - H_B^{\mathbf{k}} \right\|_{\text{F}}^2}. \quad (27)$$

In summary, the goal for correcting the MLWFs is to find a proper V matrix that constructs a new set of slab WFs that are as similar as possible to the bulk MLWFs. The overlap error and the hopping error can be used to assess the similarity between the constructed slab WFs and the bulk MLWFs. Hence, the overlap error and the hopping error are the measure of the degree of the ‘‘seamlessness’’ of the combined tight-binding model.

B. Wavefunction correction

Now, we introduce the methods we use to determine the V matrix. The first method is to find the optimal V matrix that minimizes the average overlap error. From Eq. (20), it is evident that the average overlap error can be minimized by separately optimizing each $V^{\mathbf{k}}$ matrix. In this method, the overlap matrix $A^{\mathbf{k}}$, which contains the detailed information of the Kohn-Sham wavefunctions, needs to be calculated. Hence, we call this method the ‘‘wavefunction correction.’’

We first rewrite each summand in Eq. (20) as

$$\|V^{\mathbf{k}\dagger} A^{\mathbf{k}} - I_{\text{SB}}\|_{\text{F}}^2 = \|A^{\mathbf{k}} - V^{\mathbf{k}} I_{\text{SB}}\|_{\text{F}}^2, \quad (28)$$

using the unitarity of $V^{\mathbf{k}}$. Henceforth, we temporarily omit the superscript \mathbf{k} for brevity. The above expression is minimized when

$$V I_{\text{SB}} = U \begin{bmatrix} I_B \\ 0 \end{bmatrix} W^\dagger \quad (29)$$

is satisfied²⁰, where

$$A = U \begin{bmatrix} \Sigma \\ 0 \end{bmatrix} W^\dagger \quad (30)$$

is the singular value decomposition (SVD) of A . Here, U and W are N_W^S and N_W^B dimensional square unitary matrices, respectively, and Σ is an N_W^B dimensional square diagonal matrix with the singular values of A on its diagonal. Also, we define I_B as the N_W^B dimensional identity matrix.

Since I_{SB} is a rectangular matrix that does not have a right inverse, V is not uniquely determined from Eq. (29). To settle the remaining degree of freedom, we use the fact that the underdetermined degree of freedom can be parameterized by a unitary matrix X of the form

$$X = \begin{bmatrix} I_B & 0 \\ 0 & \tilde{X} \end{bmatrix}, \quad (31)$$

where \tilde{X} is a unitary matrix of dimension $N_W^S - N_W^B$. Note that for every V that satisfies Eq. (29), VX also satisfies it. This indeterminacy can be understood as follows. If one determines $N_W^S - N_W^B$ states in the slab MLWF subspace that are orthogonal to the N_W^B bulk MLWFs, any unitary transformation among them obviously does not change the average overlap error.

While the choice of X does not alter the average overlap error, it can modify the WFs at the surface principal layers. This change is problematic since the MLWFs from the top and bottom surface of the slab can be mixed and become substantially delocalized such that they can ‘see’ each other. In other words, the WFs living in the top principal layer can have non-zero hopping amplitude to the bottom principal layer, which invalidates the construction process of the semi-infinite surface tight-binding model described in Fig. 1. To avoid this possibility, we choose X so that the constructed WFs deviate as little as possible from their corresponding original

MLWFs. Concretely, we choose X that minimizes the deviation of VX from the identity, $\|VX - I_S\|_F$.

Now, we define the projection matrices $P = I_{SB}I_{SB}^\dagger$ and $Q = I_S - P$. It is straightforward that $PI_{SB} = I_{SB}$ and $QI_{SB} = 0$ hold. Using the fact that

$$\|Z\|_F^2 = \|ZP\|_F^2 + \|ZQ\|_F^2 \quad (32)$$

and

$$\|Z\|_F^2 = \|PZ\|_F^2 + \|QZ\|_F^2 \quad (33)$$

holds for every matrix Z , one can show that

$$\begin{aligned} & \|VX - I_S\|_F^2 \\ &= \|VP - P\|_F^2 + \|VXQ - Q\|_F^2 \\ &= \|VP - P\|_F^2 + \|PVQ\|_F^2 + \|QVXQ - Q\|_F^2. \end{aligned} \quad (34)$$

Since the first two terms in the third line of Eq. (34) is independent of X , it suffices to minimize the last term only. Using the property $QVXQ = QVQXQ$, one can obtain the unitary matrix X that minimizes Eq. (34) from the SVD of QVQ inside the Q subspace²¹. Let's denote

$$QVQ = \begin{bmatrix} 0_B & 0 \\ 0 & \tilde{V} \end{bmatrix}, \quad (35)$$

where 0_B is the N_W^B -dimensional null matrix. With the SVD

$$\tilde{V} = U'\Sigma'W'^\dagger, \quad (36)$$

the optimal \tilde{X} [Eq. (31)] satisfies

$$\tilde{X} = W'U'^\dagger. \quad (37)$$

This fully determines X [Eq. (31)] and hence VX . We call this VX the optimal V .

In summary, in the wavefunction correction method, one finds the optimal V matrix that minimizes the average overlap error ΔS_{ave} . This is done by first finding a unitary matrix $V^{\mathbf{k}}$ that satisfies Eq. (29) using U and W^\dagger as defined in Eq. (30), and then fixing the remaining indeterminacy using Eqs. (31), (36), and (37). This procedure is repeated for each $V^{\mathbf{k}}$.

Despite its optimality, the wavefunction correction may not be easy to use in practice; the calculation of the overlap matrix A requires additional computational expense and can be problematic depending on the structure of the slab supercell and the type of the pseudopotentials, as described in Sec. II.A. Since we aim at post-processing methods that work irrespective of the computational details, we use the wavefunction correction only as a reference method to evaluate other methods.

C. Minimal correction

The first practical approach we propose is to correct only the easily tractable degrees of freedom of the MLWFs, which are the permutation order, the spin axis,

and the overall phase. We call this method “minimal correction” because the applied operations require little computational cost and are the necessary minimum to obtain a reliable tight-binding model, as will be demonstrated with real material examples in Sec. IV.A. In this method, it is assumed that the corresponding MLWFs of the bulk and the slab have almost the same orbital wavefunctions up to an overall phase. This assumption justifies the minimal correction in that only the permutation, spin, and overall phase degrees of freedom remain to be corrected.

Now, we describe the procedures in detail. First, for calculations with SOC, the minimal correction consists of three steps: pairing, spin correction, and phase correction. In the pairing step, the permutation degree of freedom is fixed by finding the best matching bulk and slab MLWF pairs. The MLWFs having the same orbital parts and orthogonal spinor parts are not distinguished in this step. The matching between the bulk and the slab MLWFs can be done by pairing the MLWFs with similar center positions.

If multiple MLWFs (other than the ones with the same orbital parts but orthogonal spinor parts) have similar centers, the “signatures”⁸ of the MLWFs are exploited to find the pairs. The signatures of an MLWF are the Fourier components of the MLWF in the plane-wave representation. Concretely, the signature $I_m(\mathbf{G})$ of an MLWF $|w_{0m}\rangle$ for a given reciprocal lattice vector \mathbf{G} is

$$I_m(\mathbf{G}) = \frac{1}{\sqrt{V_{\text{cell}}}} \int_{V_{\text{cell}}} d\mathbf{r} e^{-i\mathbf{G}\cdot(\mathbf{r}-\mathbf{r}_c)} \langle \mathbf{r} | w_{0m} \rangle. \quad (38)$$

Here, \mathbf{r}_c is the center of the MLWF $|w_{0m}\rangle$. In practice, the signatures of the MLWFs are calculated for a few \mathbf{G} vectors close to $\mathbf{0}$. We calculated WF signatures at five \mathbf{G} 's: $(0,0,0)$, $(\pm 1,0,0)$, and $(0,\pm 1,0)$ in the reciprocal lattice coordinate. If necessary, one can add more \mathbf{G} vectors to the list. The method we use to calculate the MLWF signatures is detailed in Appendix A.

Since the signatures of an MLWF encode its orbital character, one can use the signatures to pair the MLWFs. For example, assume that a p_x -orbital-like MLWF and a p_y -orbital-like MLWF are centered at the same atom. The two WFs can be distinguished using the following signature

$$\begin{aligned} & I_m(\mathbf{G}_x) - I_m(-\mathbf{G}_x) \\ &= \frac{-2i}{\sqrt{V_{\text{cell}}}} \int_{V_{\text{cell}}} d\mathbf{r} \sin\left(\frac{x-x_c}{L_x}\right) \langle \mathbf{r} | w_{0m} \rangle, \end{aligned} \quad (39)$$

where $\mathbf{G}_x = 2\pi/L_x \hat{x}$. Obviously, the absolute value of this quantity of a p_x -like MLWF will be much larger than that of a p_y -like MLWF.

When multiple MLWFs have the same center, we manually pair the bulk and slab MLWFs with similar signatures. The validity of the constructed pairs can be judged by checking whether the average hopping error after the minimal correction is reasonably small.

The next step is the spin correction. In this step, the spin quantization axes of the bulk and the slab MLWFs

are aligned with each other. Also, the relative phases between the spin up and spin down MLWFs of the bulk and the slab are made equal. This is done by calculating the matrix elements of the spin operator in the MLWF basis. For MLWFs $|w_+\rangle$ and $|w_-\rangle$ that have almost the same orbital wavefunction but mutually orthogonal spinors, let us write the matrix elements of the spin angular momentum operator \mathbf{S} as

$$\mathbf{S}_{\sigma,\sigma'} = \langle w_\sigma | \mathbf{S} | w_{\sigma'} \rangle, \quad (40)$$

where $\sigma, \sigma' \in \{+, -\}$. The diagonal matrix elements, $\mathbf{S}_{+,+}$ and $\mathbf{S}_{-,-}$, are the expectation values of the spin polarization of the MLWFs. Especially, the orientation of this expectation value is of our interest. The relative phase between $|w_+\rangle$ and $|w_-\rangle$ can be calculated from the off-diagonal matrix elements $\mathbf{S}_{+,-}$. We note that the spin matrix elements can be calculated using the Wannier90 package²². After the two, opposite spin orientations and the relative phase for each such $|w_+\rangle$ and $|w_-\rangle$ of the bulk and the slab MLWFs are calculated, one can multiply an appropriate block-diagonal unitary matrix composed of 2×2 spin-rotational unitary matrices to the V matrix so that the spinor parts of the bulk and the corresponding slab MLWFs become the same. However, the two states in the slab may still have a different common overall phase than the corresponding two states in the bulk.

The last step of the minimal correction is the phase correction. Here, the common overall phase of the MLWFs $|w_+\rangle$ and $|w_-\rangle$ is calculated from their signatures. Consider two bulk MLWFs $|w_+\rangle$ and $|w_-\rangle$ and the corresponding two slab MLWFs which are paired with those bulk MLWFs in the pairing step. After the spin correction step, these bulk and slab MLWFs differ only by a single overall phase. Now, let $I_\sigma^B(\mathbf{G})$ and $I_\sigma^S(\mathbf{G})$ be the signatures of the bulk and slab MLWFs, respectively, where $\sigma \in \{+, -\}$ is the spinor index. Then, the difference of the overall phase between the bulk and the slab MLWFs can be approximated as

$$\phi = \arg \sum_{\mathbf{G}, \sigma} I_\sigma^B(\mathbf{G}) I_\sigma^S(\mathbf{G})^*, \quad (41)$$

where $\arg x$ is the argument of a complex number x . Note that the sum runs only over the five \mathbf{G} vectors for which the MLWF signatures are calculated. By multiplying the two slab MLWFs by $e^{i\phi}$, one can make the overall phase of the two slab MLWFs identical to the overall phase of the two bulk MLWFs. This finishes the correction of the permutation, spinor, and phase degrees of freedom.

For systems without SOC, the spin correction is omitted. This also holds for systems with collinear magnetism, since the spin up and spin down WFs are completely decoupled. If one assumes that the MLWFs are real-valued functions, one has to determine only the overall sign, not the overall phase of the MLWFs. We note that this simplified correction scheme based on the sign determination is implemented in the transport module of the Wannier90 package⁸. However, even spinless MLWFs

can in principle have a complex overall phase, so we do not skip the phase correction.

One may skip the spin correction for systems with SOC if the spin orientations of the MLWFs remain unchanged from those of the initial guesses (which are equally set for the pair MLWFs in the bulk and in the slab) during the process of maximal localization. This is the case for all the materials we have tested which are all non-magnetic. However, this assumption may break down for materials with strong SOC or noncollinear magnetism because the MLWFs may have preferred spin axes. Also, one still needs to calculate the spin matrix elements to check the validity of this assumption. Hence, we do not skip the spin correction.

The minimal correction is efficient in that it requires no additional quantities to be calculated other than the spin matrix elements and the MLWF signatures. These quantities can be easily obtained in usual Wannierization procedures with little additional computational effort. However, minimal correction is not applicable when the bulk and slab MLWFs have significantly different orbital wavefunctions, because then the bulk and slab MLWFs cannot be paired. Hence, it is necessary to use the same initial guesses for the bulk and the slab MLWFs. But we also find cases where the orbital parts of the bulk and slab MLWFs significantly differ from each other even though their initial guesses are the same. In these cases, the minimal correction is not applicable.

D. Hamiltonian correction

We now describe our second method, which is more effective and generally applicable. In this method, we minimize the average hopping error ΔH_{ave} , and we call it ‘‘Hamiltonian correction.’’ Compared to the wavefunction correction where the overlap error is minimized, the Hamiltonian correction is an approximate method. This is because while the overlap error is a direct measure of the nonorthogonality between the bulk and slab WFs, the hopping error is an indirect measure of the discrepancy between the WFs. However, as long as the slab is thick enough such that the charge density around the central principal layer of the slab is very close to the corresponding charge density of the bulk, which is the situation we are interested in anyway, this method is a good replacement of the wavefunction correction. The Hamiltonian correction does not require any quantities other than the Hamiltonian matrix elements to be calculated. Therefore, the Hamiltonian correction is more realistic and efficient than the wavefunction correction.

Now, we describe the Hamiltonian correction in detail. A direct minimization of ΔH_{ave} under only the unitarity constraint on $V^{\mathbf{k}}$ [Eq. (11)] is not desirable because the problem is badly underdetermined. To reveal this indeterminacy, we first note that ΔH_{ave} is minimized by separately minimizing each term in Eq. (27). Now, assume that $H_B^{\mathbf{k}}$ is a diagonal matrix. Then, for an arbi-

trary diagonal unitary matrix U and a square matrix M of the same dimension as U , $\|M\|_F = \|U^\dagger M U\|_F$ and $U^\dagger H_B^{\mathbf{k}} U = H_B^{\mathbf{k}}$ hold. It follows that ΔH_{ave} is invariant to the change $V^{\mathbf{k}} \rightarrow V^{\mathbf{k}} U$ for every diagonal unitary matrix U . For a general case where $H_B^{\mathbf{k}}$ is a hermitian matrix diagonalized as $H_B^{\mathbf{k}} = W^\dagger D W$, the transformation $V^{\mathbf{k}} \rightarrow V^{\mathbf{k}} W^\dagger U W$ leaves ΔH_{ave} unchanged and hence represents the indeterminacy. Since U can be arbitrarily chosen at each \mathbf{k} point, it may make $V^{\mathbf{k}}$ to vary widely among the \mathbf{k} points, and thus greatly delocalize the WFs.

To avoid this indeterminacy, we further constrain V such that $V_{\mathbf{R}m,0n} \neq 0$ only if $|w_{\mathbf{R}m}^S\rangle$ and $|w_{0n}^S\rangle$ are centered on the same atom. Assuming that all the WFs on the same atom reside in the same unit cell, this constraint implies

$$V_{\mathbf{R}i,0j} = V_{ij}^{(0)} \delta_{\mathbf{R},0}, \quad (42)$$

and

$$V_{ij}^{\mathbf{k}} = V_{ij}^{(0)}, \quad (43)$$

where $V^{(0)}$ is a square block-diagonal unitary matrix. The second equation indicates that $V^{\mathbf{k}}$ is identical for all \mathbf{k} . Each block of $V^{(0)}$ corresponds to the set of WFs localized at the same atom. This restriction greatly reduces the number of free parameters and eliminates the risk of delocalizing the WFs. Due to this block-diagonality constraint, only the Wannier functions in the center of the slab is considered during the Hamiltonian correction.

We impose this block-diagonality constraint and minimize ΔH_{ave} with respect to $V^{(0)}$. In this setting, $V^{(0)}$ is uniquely determined up to a single overall phase common to all WFs. This phase does not make any difference in the calculated physical quantities such as the spectral function.

There may be cases in which the WFs are not centered on the atoms, like the bonding and anti-bonding orbitals. In such cases, the block-diagonality constraint may be modified so that only the blocks of $V^{(0)}$ between MLWFs with similar centers are allowed to be nonzero.

We note that, by construction, the block-diagonal unitary matrix $V^{(0)}$ cannot take the mixing of WFs located at different positions into account. A hypothetical problematic example for our restriction on $V^{(0)}$ will be the case of diamond in which the bulk MLWFs are atom-centered sp^3 orbitals, while the slab MLWFs are bonding and anti-bonding orbitals. To reconstruct bonding and anti-bonding orbitals from the atomic sp^3 orbitals, sp^3 orbitals localized at different atoms need to be linearly combined, which is forbidden in our scheme. However, this hypothetical example of bonding and anti-bonding MLWFs of diamond is not of our concern because the bonding and anti-bonding orbitals will change into the sp^3 orbitals during maximal localization.

To minimize ΔH_{ave} under the unitarity constraint, we use the Riemannian steepest descent method introduced in Ref.²³. The detailed algorithm is explained in Appendix B. The initial condition for the steepest descent

minimization is chosen to be the output of the minimal correction. When the minimal correction is not applicable, the identity matrix is used as the initial guess for $V^{(0)}$.

In an actual correction procedure, the summation over indices i and j in Eq. (22) may run over WFs other than the ones in one principal layer of the bulk and the corresponding WFs in the central principal layer of the slab. In general, one can include additional atomic layers outside the central principal layer of the slab, and accordingly outside the corresponding principal layer of the bulk to compute ΔH_{ave} . The corresponding optimal $V^{(0)}$ includes additional block-diagonal parts for the additional atomic layers. Although these additional parts of $V^{(0)}$ are not used in the end for the combination of the two tight-binding models, this extension may still improve the performance of the correction since the atoms at the boundary and those in the middle of the central principal layer of the slab are treated on a more equal footing. In this work, we include the additional MLWFs centered at two atomic layers both right above and right below the central principal layer.

III. COMPUTATIONAL DETAILS

To demonstrate the utility of the proposed corrections, we applied them to the surfaces of four real materials: diamond, GeTe, Bi_2Se_3 , and TaAs. To perform electronic structure calculations, we used DFT with plane-wave basis as implemented in the QUANTUM ESPRESSO package²⁴. The exchange-correlation energy was treated within the generalized gradient approximation, using the parameterization scheme of Perdew, Burke, and Ernzerhof²⁵. The plane-wave energy cutoff for wavefunctions was set to 70 Ry for all materials. Fully relativistic pseudopotentials for C, Ge, and Te were taken from pslibrary.0.3.1²⁶. Those for Ta and As were taken from the SG15 library²⁷, and those for Bi and Se were generated using ld1.x atomic code of the QUANTUM ESPRESSO package²⁴. Noncollinear spin polarization and SOC were taken into account for GeTe, Bi_2Se_3 , and TaAs. Magnetism was not considered.

In all calculations, we used experimental lattice constants. The position of the atoms of the bulk structure were fully relaxed, while the structural relaxation of the surface from the bulk structure was intentionally not taken into account for a clear comparison of the results obtained from different methods. The surface we studied are (111) surface of diamond with dangling bonds, Te-terminated (111) surface of GeTe, (0001) surface of Bi_2Se_3 which is the natural cleavage surface, and As-terminated (001) surface of TaAs. For diamond, GeTe, Bi_2Se_3 , and TaAs, the bulk principal layers are consisted of 6, 6, 15, and 8 atoms, respectively, and the slab supercells contain 42, 31, 40, and 40 atoms, respectively. For self-consistent calculation of the electronic structures, we sampled the Brillouin zone with a uniform $12 \times 12 \times n_3$

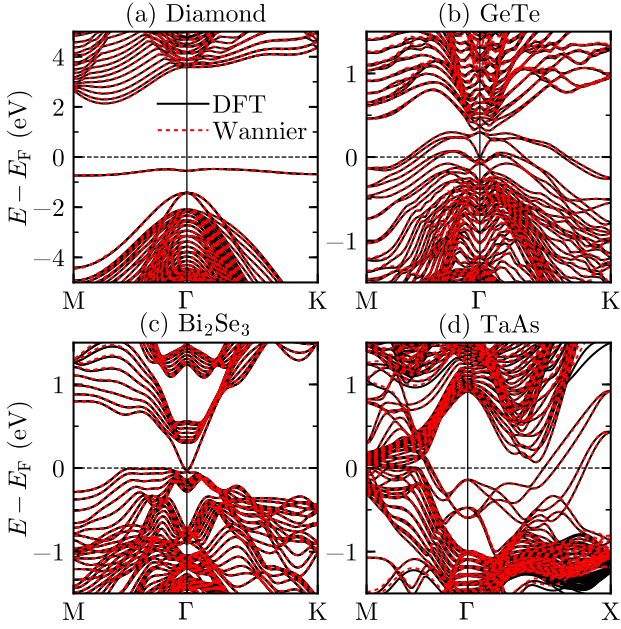


FIG. 2. The band structures of the slabs obtained by DFT and by Wannier interpolation.

mesh for the bulk, and $12 \times 12 \times 1$ mesh for the slab. The parameter n_3 was set to 11, 6, 3, and 8 for diamond, GeTe, Bi_2Se_3 , and TaAs, respectively.

We used Wannier90 package²² to construct the MLWFs. During this procedure, the Brillouin zone was sampled with uniform $7 \times 7 \times n'_3$ and $7 \times 7 \times 1$ meshes for the bulk and the slab respectively, where $n'_3=9, 6, 3$, and 6 for diamond, GeTe, Bi_2Se_3 , and TaAs, respectively. The initial guesses for the construction of the MLWFs were atom-centered sp^3 orbitals for diamond, s and p orbitals for GeTe, p orbitals for Bi_2Se_3 , and Ta-centered d orbitals and As-centered p orbitals for TaAs. For spin noncollinear systems, the spinor part of the initial guess orbitals were aligned along the z axis, unless otherwise specified. The inner frozen windows were set to $[-1, 1]$ eV around the Fermi level. For insulators, the Fermi level was defined as the average of the valence band maximum and conduction band minimum energy. The outer disentanglement windows were set to $[-\infty, +15]$, $[-\infty, +10]$, $[-7, 13]$, and $[-9.5, 9.5]$ eV for diamond, GeTe, Bi_2Se_3 , and TaAs, respectively. Here, $-\infty$ indicates that the lower bound for the window was not set. The energy windows were chosen so that the unbound states of the slab were excluded from the frozen window, and the bands that were not used for Wannierization were excluded from the disentanglement window.

Figure 2 shows that the *ab initio* tight-binding models of the slab based on MLWFs accurately describe the band structure obtained from the DFT calculations inside the inner frozen energy window. The minimal or the Hamiltonian correction to the slab tight-binding model for combination with the bulk tight-binding model is a unitary transformation common to all k points in the

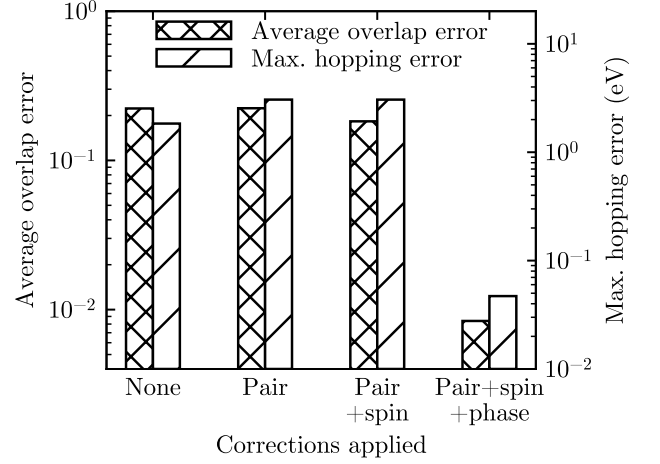


FIG. 3. The overlap and hopping errors for Bi_2Se_3 as pairing, spin correction, and phase correction are applied sequentially. The spin of the initial guesses for the bulk and slab MLWFs are aligned along the x and the z axes, respectively.

coarse grid. Therefore, the energy eigenvalues are not affected by the minimal or the Hamiltonian correction. In contrast, the wavefunction correction applies different unitary transformation to each k point in the coarse grid. Thus, the energy eigenvalues of the tight-binding model at k points which do not belong to the coarse k -point mesh used to generate the MLWFs are also changed. We find that for all the materials we have tested, this change in the energy eigenvalues is less than 14 meV. Since this change is not noticeable in the scale of Fig. 2, we have presented only the band structure obtained from the *ab initio* tight-binding models of the slab before any correction.

IV. APPLICATIONS

Now we illustrate the application of our post-processing corrections to the surfaces of diamond, GeTe, Bi_2Se_3 , and TaAs. Diamond is chosen to represent materials with strong covalent bonding. For other three materials, GeTe^{28–30}, Bi_2Se_3 ^{9,31}, and TaAs^{32–35}, SOC have significant effects on their electronic structures, and their surface states are being actively investigated.

A. Minimal correction

We first investigate the performance of the minimal correction. In Fig. 3, we show the change of the overlap and hopping errors of Bi_2Se_3 as the three steps of minimal correction, pairing, spin correction, and phase correction, are applied sequentially. To mimic the case in which the spin axis of the MLWFs considerably differ from that of the initial guesses, for example, complex materials with strong SOC or noncollinear magnetism, we align the spin

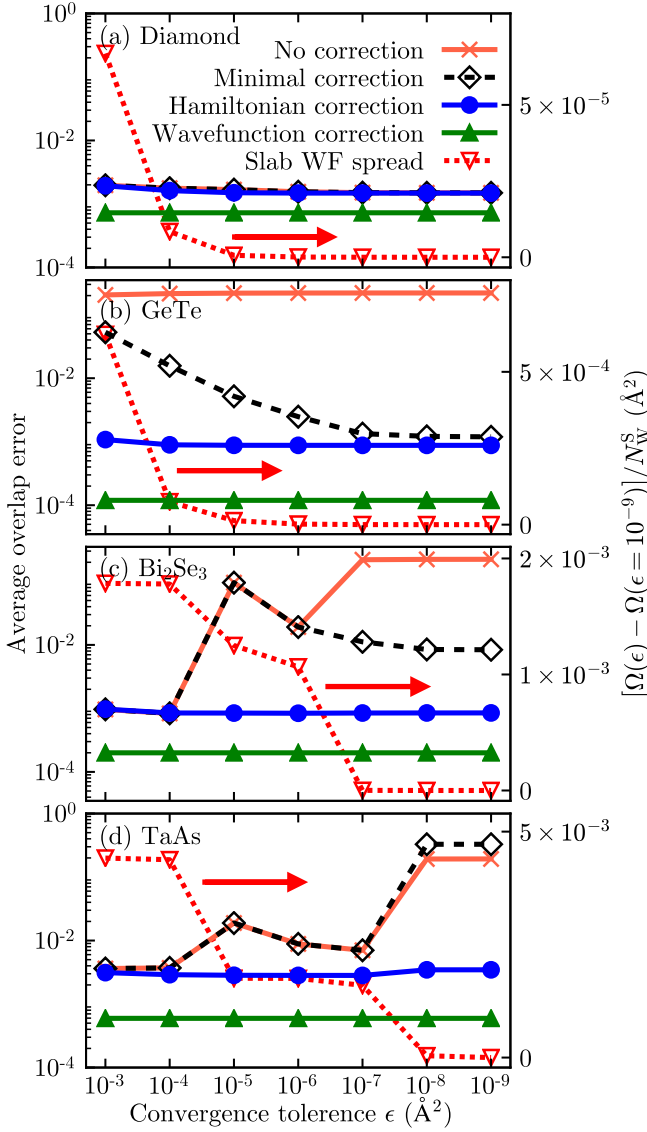


FIG. 4. Dependence of the average overlap error and the WF spread of the slab upon convergence criterion, parameterized by the convergence tolerance ϵ . The total spread is normalized by dividing it with the number of MLWFs. Lines are a guide to the eye.

orientations of the initial guesses of the bulk MLWFs along the x axis, and that of the slab MLWFs along the z axis.

We find that the overlap and hopping errors are reduced only if all the three steps are applied. The residual maximum hopping error after the minimal correction is less than 3% of a typical nearest neighbor hopping energy, indicating that the bulk and slab tight-binding models are properly combined. This result justifies our naming of the minimal correction, as it is the smallest set of corrections required for the seamless stitching of tight-binding models based on MLWFs.

In Fig. 4, we show the dependence of the overlap error

and the final WF spread Ω on the convergence criterion. In the Wannier90 package²², the convergence criterion is controlled by a parameter called convergence tolerance ϵ ; convergence is reached when the change in Ω per each iteration is less than ϵ for five successive iterations. For all the systems we have tested, the overlap and hopping errors calculated for the MLWFs obtained with $\epsilon < 10^{-9}$ do not show noticeable change in the scale shown in Fig. 4 from those calculated for the MLWFs obtained with $\epsilon = 10^{-9}$. We plot the difference between Ω at given ϵ and the value of Ω at $\epsilon = 10^{-9}$ for the slab MLWFs in Fig. 4. The spread Ω is normalized by dividing it by N_W^S .

For Bi_2Se_3 and TaAs, the overlap error is small even without any correction if a sufficiently loose convergence criterion is used ($\epsilon \geq 10^{-4}$). However, this case with large ϵ is not of our interest because the constructed MLWFs are not localized enough, as the large value of $\Omega(\epsilon)$ indicates.

We focus on the regime of sufficiently small ϵ , where Ω has almost converged. In this regime, the average overlap error of the MLWFs of diamond, the simplest material among the four we studied, is almost insensitive to the convergence threshold and is close to its minimal value obtained with the wavefunction correction. In contrast, for GeTe, the overlap error without any correction is markedly large for all values of ϵ . The error is significantly reduced by the minimal correction, especially when ϵ is small. A similar tendency shows up in the case of Bi_2Se_3 , where the overlap error is sizable without correction but is reduced by a few orders of magnitude after the minimal correction. Also, as in the case of GeTe, the overlap error after minimal correction decreases as ϵ is lowered. This result indicates that the orbital parts of the bulk and slab MLWFs become similar with a tight convergence criterion. Thus, a sufficiently tight convergence criterion is required for the minimal correction to be effective.

On the contrary, in the case of TaAs, the minimal correction fails if $\epsilon \leq 10^{-8}$ as the large overlap error indicates. Upon inspection of the center position of the MLWFs, we find that for the bulk all 10 MLWFs corresponding to the Ta d orbitals are precisely centered at the Ta atom. In contrast, for the slab, 4 out of 10 corresponding MLWFs are shifted from the Ta site by 0.17 Å. This difference signifies that the orbital parts of the bulk and slab MLWFs that correspond to the Ta d orbitals have significant differences, breaking the fundamental assumption of the minimal correction. Therefore, the minimal correction cannot be applied in this case.

In summary, the minimal correction is the smallest set of procedures required to obtain a reliable combined tight-binding model. This method is simple and efficient, given that a sufficiently tight convergence criterion for localization is used. However, the minimal correction may not work when the orbital parts of the bulk and slab MLWFs significantly differ from each other. Therefore, it is desirable to have a more generally useful correction method.

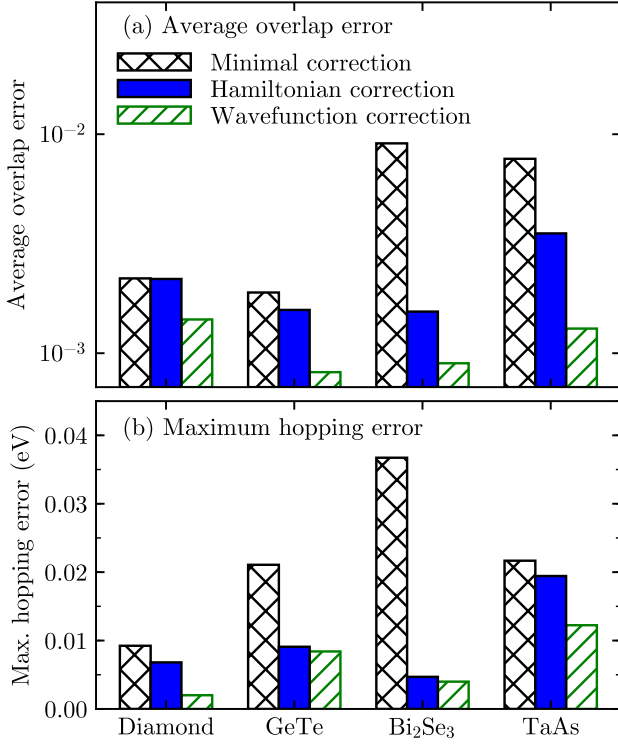


FIG. 5. The (a) average overlap error and (b) maximum hopping error for different materials after either minimal, Hamiltonian, or wavefunction correction.

B. Hamiltonian correction

We now turn to the analysis of the Hamiltonian correction which is proposed to be a widely applicable and accurate. Figure 4 shows that the overlap error after Hamiltonian correction is consistently low for all materials in the entire range of ϵ . This result demonstrates that the overlap error between MLWFs localized at the same atom gives significant contribution to the average overlap error. This error is successfully fixed by the Hamiltonian correction, while cannot be handled by the minimal correction in some cases.

We further investigate the effect of Hamiltonian correction on the overlap and the hopping errors. As we aim to compare the outcomes of the minimal correction and the Hamiltonian correction, we choose ϵ to be the smallest in so far as the minimal correction does not fail. Concretely, $\epsilon = 10^{-7}$ was used for TaAs, and $\epsilon = 10^{-9}$ was used for all other materials.

In Fig. 5, we show the average overlap error and the maximum hopping error for the four materials we have tested. The overlap error after the Hamiltonian correction is significantly smaller than the overlap error after the minimal correction. Since the Hamiltonian correction minimizes the average hopping error not the average overlap error, the decrease of the latter is a non-trivial result, albeit expected. The hopping error is also consistently reduced after the Hamiltonian correction, and even

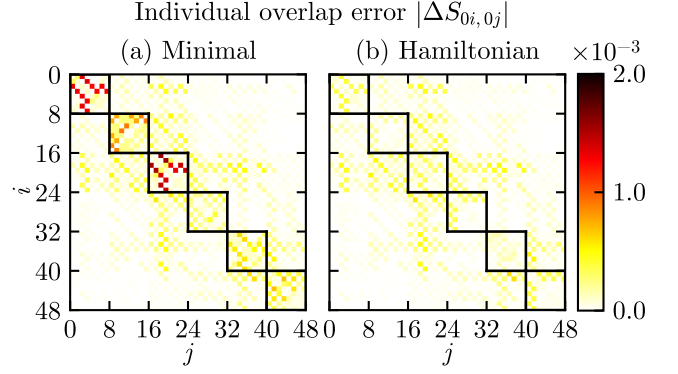


FIG. 6. Individual overlap errors of GeTe as defined in Eq. (13) calculated between WFs in the same unit cell. The WFs are corrected using (a) the minimal correction or (b) the Hamiltonian correction. The block diagonal boxes indicate the WFs centered at the same atom.

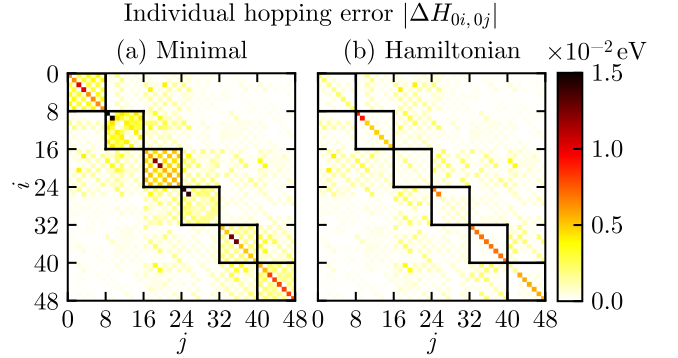


FIG. 7. Individual hopping errors of GeTe as defined in Eq. (21) calculated between WFs in the same unit cell. The WFs are corrected using (a) the minimal correction or (b) the Hamiltonian correction. The block diagonal boxes indicate the WFs centered at the same atom.

becomes comparable to the reference value obtained from the wavefunction correction in most cases. The maximal hopping error after the Hamiltonian correction is less than 1% of the typical hopping matrix element between MLWFs centered at nearest neighboring atoms.

For further analysis, we show in Fig. 6 the individual overlap errors between MLWFs that belong to the same unit cell for GeTe. We indicate the matrix elements between MLWFs centered at the same atom using the block diagonal boxes. While there are certain individual overlap errors relatively bigger than others after only the minimal correction, all of them are much reduced after applying the Hamiltonian correction. This reduction in error visually demonstrates that the Hamiltonian correction successfully corrects the dominant source of overlap error.

In Fig. 7, we show an analogous plot for the individual hopping errors. Again, the individual hopping errors remaining after the minimal correction are significantly

reduced by the Hamiltonian correction. Majority of the remaining hopping errors shown in Fig. 7(b) are the shift of the on-site energy. We attribute this error to the effect of the surface, making the potential energy at the center of the slab differ from that of the bulk. This error could be systematically reduced if the *ab initio* tight-binding model is generated using a thicker slab.

C. Calculation of the momentum-resolved surface local density of states

Now, we investigate the effects of inaccurate stitching of the MLWFs on actual physical quantities calculated from the combined tight-binding model for the surface. In Fig. 8, we show the momentum-resolved bulk and surface density of states (DOS) calculated from the semi-infinite surface using the iterative method for obtaining the Green function¹⁵.

We find that the momentum-resolved surface DOS calculated from the bulk-derived surface model, i.e., by using the surface tight-binding model constructed by using exactly the same on-site potentials and hopping integrals as the bulk, significantly deviates from the momentum-resolved surface DOS calculated from slab-derived models. This result demonstrates the importance of properly taking into account the deviation of the electronic structure at surfaces from that of the bulk in surface simulations.

Also, we find in Fig. 8 that for some materials, if no correction is applied, or if only the minimal correction is applied, bands that do not occur in case of the Hamiltonian correction appear in the momentum-resolved surface DOS. The black arrows in Figs. 8(m), 8(w), and 8(x) indicate these additional bands. From these considerations, we conclude that the additional bands are non-physical impurity bands, created due to the erroneous stitching of the bulk and slab MLWFs. These bands are a direct evidence showing that improper stitching of the bulk and slab MLWFs can lead to artifacts in the physical quantities calculated from the combined tight-binding model.

In the case of TaAs, we find that the non-physical bands occur only when $\epsilon \leq 10^{-8}$. Note that the occurrence of these bands are likely be related with the large jump in the average overlap error at $\epsilon = 10^{-8}$ shown in Fig. 4(d). The non-physical bands are not removed after the minimal correction. On the contrary, the momentum-resolved surface DOS for $\epsilon = 10^{-7}$ and $\epsilon = 10^{-9}$ with the Hamiltonian correction are indistinguishable. These results show that the Hamiltonian correction can effectively reduce the errors that occur during maximal localization, even when minimal correction fails to do so.

Using our methods, we have also generated the tight-binding models of diamond, GeTe, and Bi₂Se₃ slabs thicker than the ones used for the seamless stitching and found that their energy eigenvalues are in excellent agreement with those obtained from a direct DFT calculations on the corresponding thicker slabs (not shown). This test

demonstrates the validity of our methods.

V. COMPARISON WITH THE PROJECTION-ONLY WANNIER FUNCTIONS

Finally, we compare the Hamiltonian corrected MLWFs with the projection-only WFs. Projection-only WFs are constructed by projecting the initial guesses to the target subspace of Kohn-Sham eigenstates, and then applying Löwdin orthogonalization. The target subspace can be determined either with¹⁰ or without^{4,5,36,37} the disentanglement step, where the gauge-invariant part of Ω is iteratively minimized². The gauge-variant part of Ω however is not further minimized.

Since the projection-only WFs retain the atomic-orbital-like features of the initial guesses, projection-only WFs obtained from different systems tend to be similar. Thus, they can be used as the basis functions to combine *ab initio* tight-binding models without further correction.

In Fig. 9, we show the average overlap error and the maximal hopping error obtained from the corrected MLWFs and the projection-only WFs. First of all, the projection-only WFs without disentanglement result in much larger errors than those with disentanglement. Therefore, for a fair comparison, we exclude the case of projection-only WFs without disentanglement in the following discussion. While the errors of the MLWFs after the minimal correction are much larger than the others, the errors after the Hamiltonian correction are comparable to those of the projection-only WFs. We note that the minimal and the Hamiltonian corrections have no effect on the projection-only WFs.

For further investigation, we look for the dominant sources of the overlap errors. In Fig. 10, we show for GeTe the cumulative sum of individual overlap errors as a function of the distance between the centers of the WFs. In the case of minimal correction, around half of the overlap error originates from the WFs whose centers are closer than the bond length. In other words, the nonorthogonality between the bulk and slab MLWFs centered on the same atom is the dominant source of error.

In the case of Hamiltonian correction, the nonorthogonality between MLWFs centered on the same atom is almost completely suppressed. Instead, overlap between MLWFs centered on nearby atoms are dominant. The MLWFs whose centers are separated by longer than 10 Å make negligible contribution to the average overlap error, reflecting the locality of MLWFs.

Contrary to the previous two cases, the overlap error between the projection-only WFs comes from a broad range of WF center distance, from 3 to 20 Å. The projection-only WFs are less localized than the MLWFs and have non-negligible overlap even if the centers of the WFs are separated far apart.

An advantage of using projection-only WFs is that one can generate a tight-binding model having the symmetry of the system, such as discrete rotational symme-

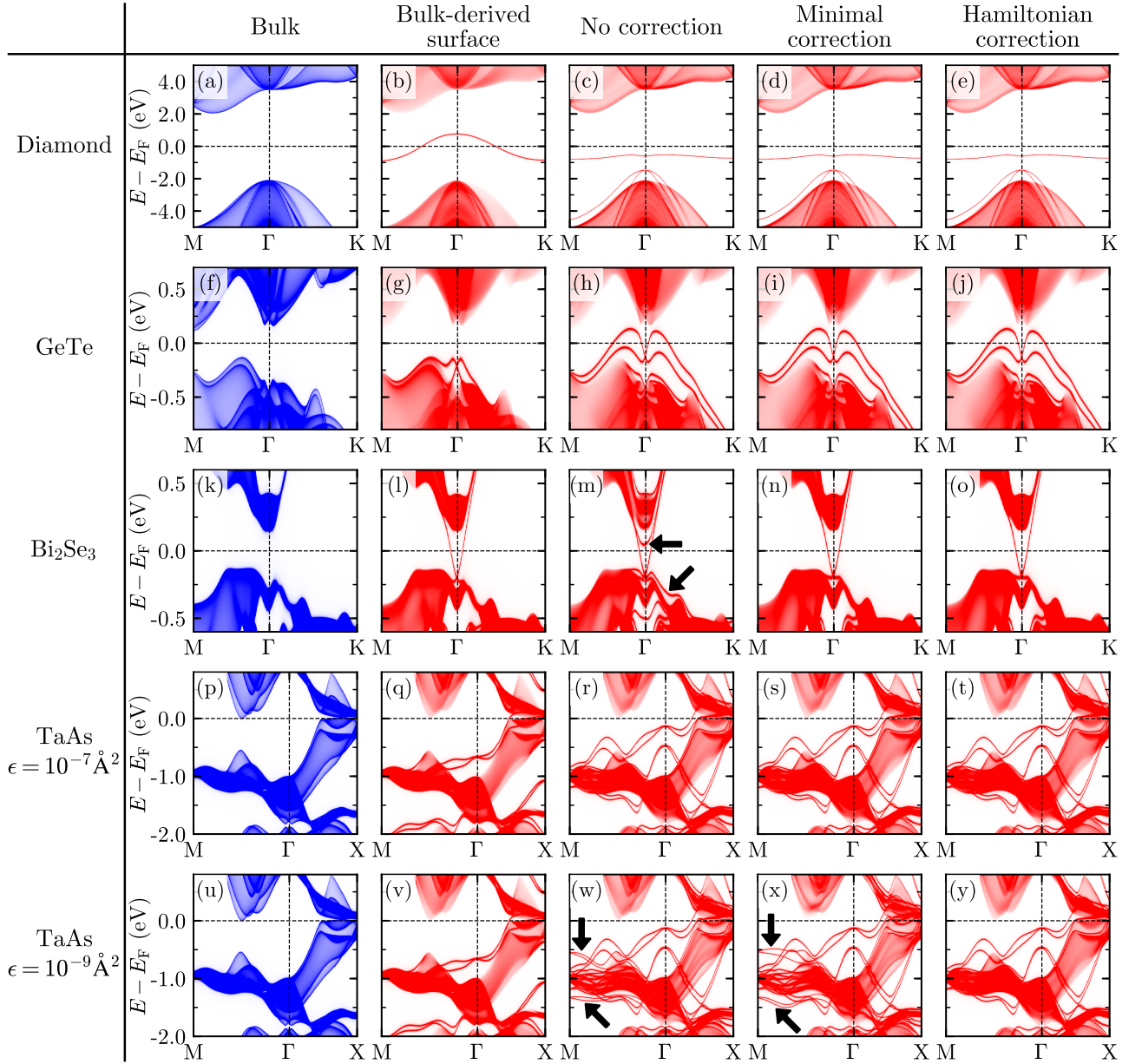


FIG. 8. Momentum-resolved (a) bulk and (b)-(e) surface DOS of diamond obtained by iterative calculations of Green functions of semi-infinite surfaces. The semi-infinite surface is either (b) derived from the bulk tight-binding parameters, (c) derived from the slab without any correction, (d) derived from the slab with the minimal correction, or (e) derived from the slab with the Hamiltonian correction. Similar quantities as in (a)-(e) for (f)-(j) GeTe, (k)-(o) Bi₂Se₃ (all with $\epsilon = 10^{-9}$), (p)-(t) TaAs with convergence tolerance $\epsilon = 10^{-7}$, and (u)-(y) TaAs with $\epsilon = 10^{-9}$.

try. However, one can obtain MLWF-based tight-binding models with the symmetry of the electronic system by modifying the localization functional³⁸ or by explicitly imposing the symmetry³⁹. Since the corrections proposed in this paper are post-processing methods, one can apply them to these generalized MLWFs to construct combined tight-binding models based on MLWFs that preserve the symmetry.

In summary, MLWFs with Hamiltonian correction are more localized than the projection-only WFs, while hav-

ing comparable or slightly larger errors. Therefore, by using MLWFs and the Hamiltonian correction we can seamlessly stitch two tight-binding models without resorting to the similarity of the initial guesses for the bulk and the slab WFs. This combination of methods also enables to seamlessly stitch two tight-binding models obtained from the method of automatically generating MLWFs^{40,41}, in which the initial guesses for the WFs are not manually selected but are automatically constructed using only a few parameters.

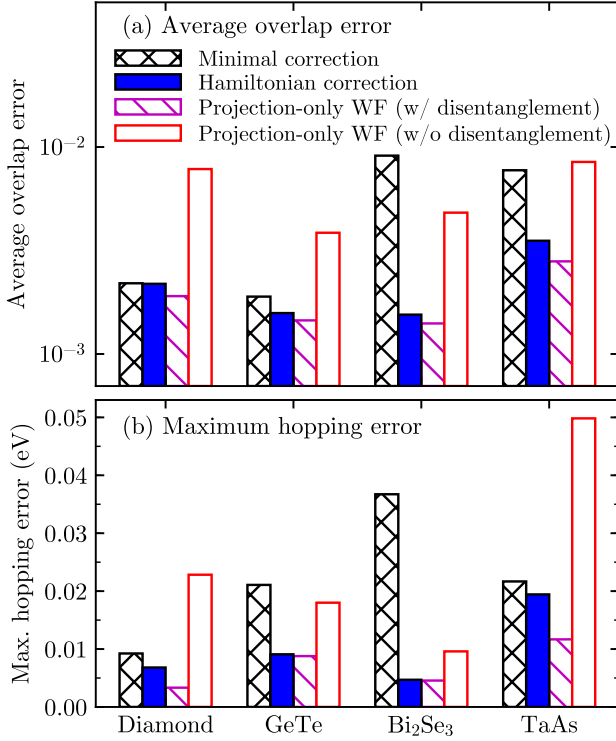


FIG. 9. The (a) average overlap error and (b) maximum hopping error for different types of WFs. For each material, the errors are calculated for MLWFs after minimal or Hamiltonian correction and for projection-only WFs, either with or without disentanglement.

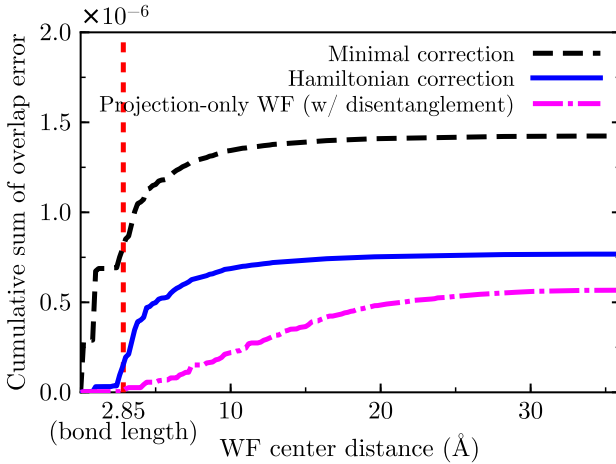


FIG. 10. The cumulative sum of squared individual overlap errors with respect to the distance between the centers of the WFs for GeTe. The vertical dashed line indicates the length of the shortest Ge-Te bond. The cumulative sum is normalized so that its square root reaches the average overlap error shown in Fig. 9(a).

In passing we note that obviously one cannot use the Hamiltonian correction if the two systems to be combined have different atomic structures in the common region where the WFs in the two systems are combined. This is because the Hamiltonian correction is based on the similarity of the Hamiltonian at the level of *ab initio* calculation. Use of WFs for band unfolding⁵, virtual crystal approximation¹², and interpolation of SOC⁴² or strain⁴³ belong to this category.

VI. CONCLUSION

In conclusion, we proposed two post-processing methods that correct the difference between MLWFs obtained from different systems. We tested our methods on the surfaces of four materials and assessed the results based on the overlap error and the hopping error. We showed that the minimal correction is successful in correcting the discrepancy between the MLWFs if the convergence criterion for the total spread is sufficiently tight, and the orbital wavefunctions of the bulk and slab MLWFs do not significantly differ from each other. However, depending on the material and on the convergence criterion, the minimal correction resulted in large overlap and hopping errors in some cases. On the other hand, the Hamiltonian correction was found to be much more accurate and generally applicable. The errors of the Hamiltonian-corrected MLWFs were comparable to that of the projection-only WFs. These corrections can be easily used in the study of surfaces, interfaces, and defects to obtain reliable results from the combined *ab initio* tight-binding models based on MLWFs.

ACKNOWLEDGMENTS

This work was supported by the Creative-Pioneering Research Program through Seoul National University.

Appendix A: Plane-wave basis methods

In this appendix, we detail the methods specific to plane-wave basis DFT calculations. Using a plane-wave basis set defined as

$$\langle \mathbf{r} | \mathbf{k} + \mathbf{G} \rangle = \frac{1}{\sqrt{V_{\text{cell}}}} e^{i(\mathbf{k} + \mathbf{G}) \cdot \mathbf{r}} \quad (\text{A1})$$

where V_{cell} is the volume of the unit cell, we can represent the Kohn-Sham eigenstates of the bulk and the slab as

$$|\psi_{j\mathbf{k}'}^{\text{B}}\rangle = \sum_{\mathbf{G}'} c_{j\mathbf{k}'\mathbf{G}'}^{\text{B}} |\mathbf{k}' + \mathbf{G}'\rangle \quad (\text{A2})$$

and

$$|\psi_{n\mathbf{k}}^{\text{S}}\rangle = \sum_{\mathbf{G}} c_{n\mathbf{k}\mathbf{G}}^{\text{S}} |\mathbf{k} + \mathbf{G}\rangle, \quad (\text{A3})$$

respectively. Here, \mathbf{k}' and \mathbf{G}' are the Bloch wavevector and the reciprocal-lattice vector of the bulk, respectively, and \mathbf{k} and \mathbf{G} are the corresponding quantities of the slab. Also, j and n are the band indices of the bulk and slab Bloch states, respectively.

To calculate the inner product between the bulk and slab wavefunctions, we choose the plane-wave bases of the bulk and the slab to be commensurate. Concretely, let the fast fourier transformation (FFT) grid for wavefunctions be $N_1 \times N_2 \times N_3$ and the k-point grid for Wannierization be $n_1 \times n_2 \times n_3$ for the bulk. Then, we choose the slab supercell to have the same in-plane lattice parameters as the bulk and set the out-of-plane lattice parameter as n_3 times the out-of-plane lattice parameter of the bulk. The FFT grid for DFT calculation and the k-point grid for Wannierization of the slab are chosen as $N_1 \times N_2 \times N_3 n_3$ and $n_1 \times n_2 \times 1$, respectively. With these choices, the inner product between the bulk and slab wavefunctions can be calculated using the inner product of the bulk and slab plane waves,

$$\langle \mathbf{k} + \mathbf{G} | \mathbf{k}' + \mathbf{G}' \rangle = \delta_{\mathbf{k}+\mathbf{G}, \mathbf{k}'+\mathbf{G}'} . \quad (\text{A4})$$

The unitary transform from the Kohn-Sham eigenstates to the MLWFs is given as

$$|w_{\mathbf{R}i}^{\mathbf{B}}\rangle = \frac{1}{\sqrt{N_{\mathbf{W}}^{\mathbf{B}}}} \sum_{\mathbf{k}', j} e^{-i\mathbf{k}' \cdot \mathbf{R}'} |\psi_{j\mathbf{k}'}^{\mathbf{B}}\rangle (U_{\mathbf{B}}^{\mathbf{k}'})_{ji} \quad (\text{A5})$$

and

$$|w_{\mathbf{R}m}^{\mathbf{S}}\rangle = \frac{1}{\sqrt{N_{\mathbf{W}}^{\mathbf{S}}}} \sum_{\mathbf{k}, n} e^{-i\mathbf{k} \cdot \mathbf{R}} |\psi_{n\mathbf{k}}^{\mathbf{S}}\rangle (U_{\mathbf{S}}^{\mathbf{k}})_{nm} . \quad (\text{A6})$$

Now, we calculate the overlap matrix A defined in Eqs. (15). From Eqs. (A5) and (A6), one obtains

$$\begin{aligned} A_{\mathbf{R}m, \mathbf{0}i} &= \langle w_{\mathbf{R}m}^{\mathbf{S}} | w_{\mathbf{0}i}^{\mathbf{B}} \rangle \\ &= \frac{1}{\sqrt{N_{\mathbf{W}}^{\mathbf{B}} N_{\mathbf{W}}^{\mathbf{S}}}} \sum_{\mathbf{k}, \mathbf{k}', n, j} e^{i\mathbf{k} \cdot \mathbf{R}} (U_{\mathbf{S}}^{\mathbf{k}\dagger})_{mn} \langle \psi_{n\mathbf{k}}^{\mathbf{S}} | \psi_{j\mathbf{k}'}^{\mathbf{B}} \rangle (U_{\mathbf{B}}^{\mathbf{k}'})_{ji} . \end{aligned} \quad (\text{A7})$$

From Eqs. (16), (A4), and (A7), one obtains

$$\begin{aligned} A_{mi}^{\mathbf{k}} &= \sum_{\mathbf{R}} e^{-i\mathbf{k} \cdot \mathbf{R}} A_{\mathbf{R}m, \mathbf{0}i} \\ &= \sqrt{\frac{N_{\mathbf{W}}^{\mathbf{S}}}{N_{\mathbf{W}}^{\mathbf{B}}}} \sum_{\mathbf{k}', n, j} (U_{\mathbf{S}}^{\mathbf{k}\dagger})_{mn} \langle \psi_{n\mathbf{k}}^{\mathbf{S}} | \psi_{j\mathbf{k}'}^{\mathbf{B}} \rangle (U_{\mathbf{B}}^{\mathbf{k}'})_{ji} \\ &= \sqrt{\frac{N_{\mathbf{W}}^{\mathbf{S}}}{N_{\mathbf{W}}^{\mathbf{B}}}} \sum_{\mathbf{k}', \mathbf{G}, \mathbf{G}'} \sum_{n, j} (U_{\mathbf{S}}^{\mathbf{k}\dagger})_{mn} c_{n\mathbf{k}\mathbf{G}}^{S*} c_{j\mathbf{k}'\mathbf{G}'}^{\mathbf{B}} (U_{\mathbf{B}}^{\mathbf{k}'})_{ji} \delta_{\mathbf{k}+\mathbf{G}, \mathbf{k}'+\mathbf{G}'} . \end{aligned} \quad (\text{A8})$$

Note that the sum over \mathbf{k}' is calculated only over those having the same in-plane component as \mathbf{k} , since otherwise $\langle \psi_{n\mathbf{k}}^{\mathbf{S}} | \psi_{j\mathbf{k}'}^{\mathbf{B}} \rangle = 0$. From Eq. (A8), the overlap matrix $A_{mi}^{\mathbf{k}}$ can be calculated from the $c_{\mathbf{G}}$ coefficients and the U matrices, which are obtained from the *ab initio* calculation and Wannierization, respectively.

Next, we explain the calculation of WF signatures used in the minimal correction. WF signatures are the coefficients of the WFs in the plane-wave basis, as defined in Eq. (38). It can be straightforwardly calculated using Eqs. (A1), (A3), and (A6) for the slab,

$$\begin{aligned} I_m^{\mathbf{S}}(\mathbf{G}) &= \frac{1}{\sqrt{V_{\text{cell}}}} \int_{V_{\text{cell}}} d\mathbf{r} e^{-i\mathbf{G} \cdot (\mathbf{r} - \mathbf{r}_c)} \langle \mathbf{r} | w_{\mathbf{0}m} \rangle \\ &= e^{i\mathbf{G} \cdot \mathbf{r}_c} \langle \mathbf{G} | w_{\mathbf{0}m} \rangle \\ &= \frac{1}{\sqrt{N_{\mathbf{W}}^{\mathbf{S}}}} e^{i\mathbf{G} \cdot \mathbf{r}_c} \sum_{\mathbf{k}} \langle \mathbf{G} | \psi_{n\mathbf{k}}^{\mathbf{S}} \rangle (U_{\mathbf{S}}^{\mathbf{k}})_{nm} \\ &= \frac{1}{\sqrt{N_{\mathbf{W}}^{\mathbf{S}}}} e^{i\mathbf{G} \cdot \mathbf{r}_c} \sum_n c_{n\mathbf{0}\mathbf{G}}^{\mathbf{S}} (U_{\mathbf{S}}^{\mathbf{0}})_{nm} , \end{aligned} \quad (\text{A9})$$

and analogously for the bulk,

$$I_i^{\mathbf{B}}(\mathbf{G}') = \frac{1}{\sqrt{N_{\mathbf{W}}^{\mathbf{B}}}} e^{i\mathbf{G}' \cdot \mathbf{r}_c} \sum_j c_{j\mathbf{0}\mathbf{G}'}^{\mathbf{B}} (U_{\mathbf{B}}^{\mathbf{0}})_{ji} . \quad (\text{A10})$$

Note that only the plane-wave coefficients for $\mathbf{k} = \mathbf{0}$ is used.

If the out-of-plane lattice constant of the slab supercell is not an integer multiple of that of the bulk, one cannot compare the bulk and slab WF signatures corresponding to a \mathbf{G} vector with nonzero out-of-plane component. Since our minimal correction aims at working irrespective of the supercell structure, we do not use signatures at \mathbf{G} vectors with nonzero out-of-plane component during corrections.

In practice, we use the WF signatures at five \mathbf{G} vectors: $\mathbf{G} = (0,0,0)$, $(\pm 1,0,0)$, and $(0,\pm 1,0)$, in units of reciprocal lattice vectors. We find these \mathbf{G} vectors sufficient for all the materials we have tested, but it is possible to increase the number of \mathbf{G} vectors if necessary. Since the WF signatures are calculated for only a few \mathbf{G} vectors, the required computational cost is negligible.

Appendix B: Steepest descent minimization algorithm

In this appendix, we explain the steepest descent algorithm we use for the Hamiltonian correction. The Hamiltonian correction is achieved by finding the optimal $V^{(0)}$ matrix, common to all \mathbf{k} , that minimizes the square of the average hopping error

$$\Delta H_{\text{ave}}^2 [V^{(0)}] = \frac{1}{N_{\mathbf{W}}^{\mathbf{B}} N_{\mathbf{k}}^{\mathbf{S}}} \sum_{\mathbf{k}} \left\| V^{(0)\dagger} H_{\mathbf{S}}^{\mathbf{k}} V^{(0)} - H_{\mathbf{B}}^{\mathbf{k}} \right\|_{\text{F}}^2 \quad (\text{B1})$$

under the constraint that $V^{(0)}$ is a block-diagonal unitary matrix. Matrices $H_{\mathbf{S}}^{\mathbf{k}}$ and $H_{\mathbf{B}}^{\mathbf{k}}$ are square hermitian matrices of dimension $N_{\mathbf{W}}^{\mathbf{B}}$.

Hereafter in this appendix, we omit the superscript (0) in $V^{(0)}$ for brevity. Omitting the irrelevant factor

$1/N_W^B N_k^S$ from Eq. (B1) and using the unitarity of V , one can show that

$$J[V] = N_W^B N_k^S \Delta H_{ave}^2[V] \\ = \sum_k \left(\|H_S^k\|_F^2 + \|H_B^k\|_F^2 - 2 \text{Tr} V^\dagger H_S^k V H_B^k \right) \quad (\text{B2})$$

is the cost function that should be minimized. Since the first two terms in the parentheses do not depend on V , only the last term need to be considered during minimization.

To exploit the block-diagonality constraint on V , we define the projection operator P_a , which projects onto the subspace of MLWFs centered at the atom labelled with a . One can write V as a sum of blocks

$$V = \sum_a P_a V P_a = \sum_a V_a, \quad (\text{B3})$$

where we define $V_a = P_a V P_a$ as the diagonal block of V . Due to the unitarity of V , V_a is also a unitary matrix in the P_a subspace. We simultaneously optimize all V_a matrices using the steepest descent method.

The algorithm we implement is the “self-tuning Riemannian steepest descent algorithm,” as summarized in Table II of Ref. ²³. This algorithm is suitable for our purpose since the unitarity of V is explicitly maintained during the minimization steps. Hence, additional orthogonalization of the output is not needed.

In the remaining part of the appendix, we state formulae used in the algorithm. First, the gradient of the cost function is defined as

$$(\Gamma_a)_{ij} = \frac{\partial J}{\partial (V_a)_{ij}^*} = -2 \sum_k (P_a H_S^k V H_B^k P_a)_{ij}. \quad (\text{B4})$$

The gradient direction on the Riemannian space is defined as

$$G_a = \Gamma_a V_a^\dagger - V_a \Gamma_a^\dagger. \quad (\text{B5})$$

By definition, G_a is an anti-hermitian matrix.

The V_a matrix is updated by multiplying it by the update matrix Q_a defined as

$$Q_a = \exp(-\mu G_a), \quad (\text{B6})$$

with a step size parameter μ . The step size μ is a positive real number that is adaptively updated by multiplying or dividing by 2. Matrix Q_a is unitary since it is an exponential of an anti-hermitian matrix G_a . Hence, the updated matrix $Q_a V_a$ remains unitary. The set of matrices $Q_a V_a$ is used as the input V_a for the next iteration.

To determine convergence of iterations, we use the sum of the squared norm of the Riemannian gradient

$$\mathcal{N} = \frac{1}{2} \sum_a \text{Tr}(G_a G_a^\dagger). \quad (\text{B7})$$

The iteration is assumed to converge when $\mathcal{N} < N_W^B N_k^S \times 10^{-5} \text{ eV}^2$ is satisfied. In all cases we tested, at most a few tens of iterations were sufficient to reach convergence.

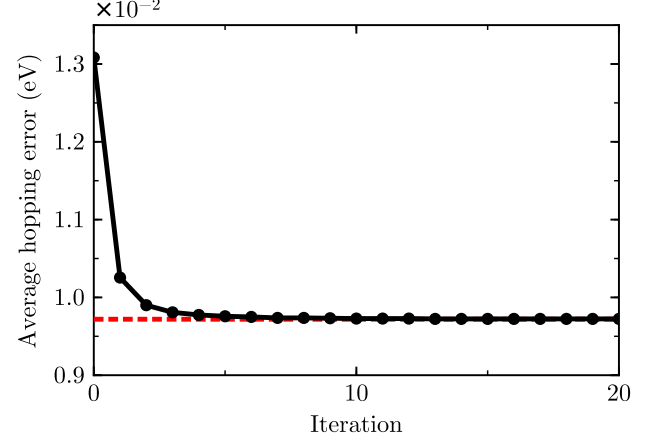


FIG. 11. The average hopping error versus the number of steepest descent iterations for the Hamiltonian correction applied to GeTe. The horizontal dashed line indicates the converged value.

We show in Fig. 11 that the average hopping error, which is proportional to the square root of the objective functional J , monotonically decreases at each iteration.

* cheolhwan@snu.ac.kr

¹ Nicola Marzari and David Vanderbilt, “Maximally localized generalized Wannier functions for composite energy bands,” *Phys. Rev. B* **56**, 12847–12865 (1997).

² Ivo Souza, Nicola Marzari, and David Vanderbilt, “Maximally localized Wannier functions for entangled energy bands,” *Phys. Rev. B* **65**, 035109 (2001).

³ Nicola Marzari, Arash A. Mostofi, Jonathan R. Yates, Ivo Souza, and David Vanderbilt, “Maximally localized Wannier functions: Theory and applications,” *Rev. Mod. Phys.* **84**, 1419–1475 (2012).

⁴ Tom Berlijn, Dmitri Volja, and Wei Ku, “Can disorder alone destroy the e'_g hole pockets of Na_xCoO_2 ? A Wannier function based first-principles method for disordered systems,” *Phys. Rev. Lett.* **106**, 077005 (2011).

⁵ Wei Ku, Tom Berlijn, and Chi-Cheng Lee, “Unfolding first-principles band structures,” *Phys. Rev. Lett.* **104**, 216401 (2010).

⁶ Arrigo Calzolari, Nicola Marzari, Ivo Souza, and Marco Buongiorno Nardelli, “Ab initio transport properties of nanostructures from maximally localized Wannier func-

- tions,” *Phys. Rev. B* **69**, 035108 (2004).
- ⁷ Young-Su Lee, Marco Buongiorno Nardelli, and Nicola Marzari, “Band structure and quantum conductance of nanostructures from maximally localized Wannier functions: The case of functionalized carbon nanotubes,” *Phys. Rev. Lett.* **95**, 076804 (2005).
 - ⁸ Matthew Shelley, Nicolas Poilvert, Arash A. Mostofi, and Nicola Marzari, “Automated quantum conductance calculations using maximally-localised Wannier functions,” *Comput. Phys. Commun.* **182**, 2174 – 2183 (2011).
 - ⁹ Haijun Zhang, Chao-Xing Liu, Xiao-Liang Qi, Xi Dai, Zhong Fang, and Shou-Cheng Zhang, “Topological insulators in Bi_2Se_3 , Bi_2Te_3 and Sb_2Te_3 with a single Dirac cone on the surface,” *Nat. Phys.* **5**, 438 (2009).
 - ¹⁰ Wei Zhang, Rui Yu, Hai-Jun Zhang, Xi Dai, and Zhong Fang, “First-principles studies of the three-dimensional strong topological insulators Bi_2Se_3 , Bi_2Te_3 and Sb_2Te_3 ,” *New J. Phys.* **12**, 065013 (2010).
 - ¹¹ Hai-Jun Zhang, Stanislav Chadov, Lukas Muehler, Binghai Yan, Xiao-Liang Qi, Jürgen Kübler, Shou-Cheng Zhang, and Claudia Felser, “Topological insulators in ternary compounds with a honeycomb lattice,” *Phys. Rev. Lett.* **106**, 156402 (2011).
 - ¹² Jianpeng Liu and David Vanderbilt, “Topological phase transitions in $(\text{Bi}_{1-x}\text{In}_x)_2\text{Se}_3$ and $(\text{Bi}_{1-x}\text{Sb}_x)_2\text{Se}_3$,” *Phys. Rev. B* **88**, 224202 (2013).
 - ¹³ Yan Sun, Shu-Chun Wu, and Binghai Yan, “Topological surface states and Fermi arcs of the noncentrosymmetric Weyl semimetals TaAs, TaP, NbAs, and NbP,” *Phys. Rev. B* **92**, 115428 (2015).
 - ¹⁴ D. H. Lee and J. D. Joannopoulos, “Simple scheme for surface-band calculations. i,” *Phys. Rev. B* **23**, 4988–4996 (1981).
 - ¹⁵ M P Lopez Sancho, J M Lopez Sancho, J M L Sancho, and J Rubio, “Highly convergent schemes for the calculation of bulk and surface Green functions,” *J. Phys. F: Metal Phys.* **15**, 851 (1985).
 - ¹⁶ David Vanderbilt, “Soft self-consistent pseudopotentials in a generalized eigenvalue formalism,” *Phys. Rev. B* **41**, 7892–7895 (1990).
 - ¹⁷ P. E. Blöchl, “Projector augmented-wave method,” *Phys. Rev. B* **50**, 17953–17979 (1994).
 - ¹⁸ Richard M Martin, *Electronic structure: basic theory and practical methods* (Cambridge university press, 2004).
 - ¹⁹ Fabiano Corsetti and Arash A. Mostofi, “System-size convergence of point defect properties: The case of the silicon vacancy,” *Phys. Rev. B* **84**, 035209 (2011).
 - ²⁰ Joseph B. Keller, “Closest unitary, orthogonal and Hermitian operators to a given operator,” *Mathematics Magazine* **48**, 192–197 (1975).
 - ²¹ Roger A Horn and Charles R Johnson, *Matrix analysis* (Cambridge university press, 1990).
 - ²² Arash A. Mostofi, Jonathan R. Yates, Giovanni Pizzi, Young-Su Lee, Ivo Souza, David Vanderbilt, and Nicola Marzari, “An updated version of wannier90: A tool for obtaining maximally-localised Wannier functions,” *Comput. Phys. Commun.* **185**, 2309 – 2310 (2014).
 - ²³ T. E. Abruđan, J. Eriksson, and V. Koivunen, “Steepest descent algorithms for optimization under unitary matrix constraint,” *IEEE Transactions on Signal Processing* **56**, 1134–1147 (2008).
 - ²⁴ P. Giannozzi, S. Baroni, N. Bonini, M. Calandra, R. Car, C. Cavazzoni, D. Ceresoli, G. L. Chiarotti, M. Cococcioni, I. Dabo, A. Dal Corso, S. de Gironcoli, S. Fabris, G. Fratesi, R. Gebauer, U. Gerstmann, C. Gougousis, A. Kokalj, M. Lazzeri, L. Martin-Samos, N. Marzari, F. Mauri, R. Mazzarello, S. Paolini, A. Pasquarello, L. Paulatto, C. Sbraccia, S. Scandolo, G. Sclauzero, A. P. Seitsonen, A. Smogunov, P. Umari, and R.M. Wentzcovitch, “QUANTUM ESPRESSO: a modular and open-source software project for quantum simulations of materials,” *J. Phys.: Condens. Matter* **21**, 395502 (2009).
 - ²⁵ John P. Perdew, Kieron Burke, and Matthias Ernzerhof, “Generalized gradient approximation made simple,” *Phys. Rev. Lett.* **77**, 3865–3868 (1996).
 - ²⁶ E. Kucukbenli, M. Monni, B. I. Adetunji, X. Ge, G. A. Adebayo, N. Marzari, S. de Gironcoli, and A. Dal Corso, “Projector augmented-wave and all-electron calculations across the periodic table: a comparison of structural and energetic properties,” ArXiv e-prints (2014), [arXiv:1404.3015 \[cond-mat.mtrl-sci\]](https://arxiv.org/abs/1404.3015).
 - ²⁷ P. Scherpezel, M. Govoni, I. Hamada, and G. Galli, “Implementation and validation of fully relativistic GW calculations: Spin-orbit coupling in molecules, nanocrystals, and solids,” *J. Chem. Theory Comput.* **12**, 3523–3544 (2016).
 - ²⁸ Marcus Liebmann, Christian Rinaldi, Domenico Di Sante, Jens Kellner, Christian Pauly, Rui Ning Wang, Jos Emiel Boschker, Alessandro Giussani, Stefano Bertoli, Matteo Cantoni, Lorenzo Baldrati, Marco Asa, Ivana Vobornik, Giancarlo Panaccione, Dmitry Marchenko, Jaime Sanchez-Barriga, Oliver Rader, Raffaella Calarco, Silvia Picozzi, Riccardo Bertacco, and Markus Morgenstern, “Giant Rashba-type spin splitting in ferroelectric GeTe (111),” *Adv. Mater.* **28**, 560–565 (2016).
 - ²⁹ H. J. Elmers, R. Wallauer, M. Liebmann, J. Kellner, M. Morgenstern, R. N. Wang, J. E. Boschker, R. Calarco, J. Sánchez-Barriga, O. Rader, D. Kutnyakhov, S. V. Chernov, K. Medjanik, C. Tusche, M. Ellguth, H. Volfava, St. Borek, J. Braun, J. Minár, H. Ebert, and G. Schönhense, “Spin mapping of surface and bulk Rashba states in ferroelectric α -GeTe(111) films,” *Phys. Rev. B* **94**, 201403 (2016).
 - ³⁰ J. Krempaský, S. Muff, J. Minár, N. Pilet, M. Fanciulli, A. P. Weber, E. B. Guedes, M. Caputo, E. Müller, V. V. Volobuev, M. Gmitra, C. A. F. Vaz, V. Scagnoli, G. Springholz, and J. H. Dil, “Operando imaging of all-electric spin texture manipulation in ferroelectric and multiferroic Rashba semiconductors,” *Phys. Rev. X* **8**, 021067 (2018).
 - ³¹ Yuqi Xia, Dong Qian, David Hsieh, L Wray, Arijeet Pal, Hsin Lin, Arun Bansil, DHYS Grauer, Yew San Hor, Robert Joseph Cava, *et al.*, “Observation of a large-gap topological-insulator class with a single Dirac cone on the surface,” *Nat. Phys.* **5**, 398 (2009).
 - ³² Shin-Ming Huang, Su-Yang Xu, Ilya Belopolski, Chi-Cheng Lee, Guoqing Chang, BaoKai Wang, Nasser Alidoust, Guang Bian, Madhab Neupane, Chenglong Zhang, *et al.*, “A Weyl fermion semimetal with surface Fermi arcs in the transition metal monophosphide TaAs class,” *Nat. Commun.* **6**, 7373 (2015).
 - ³³ Hongming Weng, Chen Fang, Zhong Fang, B. A. Bernevig, and Xi Dai, “Weyl semimetal phase in noncentrosymmetric transition-metal monophosphides,” *Phys. Rev. X* **5**, 011029 (2015).
 - ³⁴ Su-Yang Xu, Ilya Belopolski, Nasser Alidoust, Madhab Neupane, Guang Bian, Chenglong Zhang, Raman Sankar, Guoqing Chang, Zhujun Yuan, Chi-Cheng Lee, Shin-Ming Huang, Hao Zheng, Jie Ma, Daniel S. Sanchez, BaoKai

- Wang, Arun Bansil, Fangcheng Chou, Pavel P. Shibayev, Hsin Lin, Shuang Jia, and M. Zahid Hasan, “Discovery of a Weyl fermion semimetal and topological Fermi arcs,” *Science* **349**, 613–617 (2015).
- ³⁵ B. Q. Lv, H. M. Weng, B. B. Fu, X. P. Wang, H. Miao, J. Ma, P. Richard, X. C. Huang, L. X. Zhao, G. F. Chen, Z. Fang, X. Dai, T. Qian, and H. Ding, “Experimental discovery of Weyl semimetal TaAs,” *Phys. Rev. X* **5**, 031013 (2015).
- ³⁶ Wei Ku, H. Rosner, W. E. Pickett, and R. T. Scalettar, “Insulating ferromagnetism in $\text{La}_4\text{Ba}_2\text{Cu}_2\text{O}_{10}$: An ab initio Wannier function analysis,” *Phys. Rev. Lett.* **89**, 167204 (2002).
- ³⁷ V. I. Anisimov, D. E. Kondakov, A. V. Kozhevnikov, I. A. Nekrasov, Z. V. Pchelkina, J. W. Allen, S.-K. Mo, H.-D. Kim, P. Metcalf, S. Suga, A. Sekiyama, G. Keller, I. Leonov, X. Ren, and D. Vollhardt, “Full orbital calculation scheme for materials with strongly correlated electrons,” *Phys. Rev. B* **71**, 125119 (2005).
- ³⁸ Runzhi Wang, Emanuel A. Lazar, Hyowon Park, Andrew J. Millis, and Chris A. Marianetti, “Selectively localized Wannier functions,” *Phys. Rev. B* **90**, 165125 (2014).
- ³⁹ R. Sakuma, “Symmetry-adapted Wannier functions in the maximal localization procedure,” *Phys. Rev. B* **87**, 235109 (2013).
- ⁴⁰ Anil Damle, Lin Lin, and Lexing Ying, “SCDM-k: Localized orbitals for solids via selected columns of the density matrix,” *J. Comput. Phys.* **334**, 1 – 15 (2017).
- ⁴¹ Anil Damle and Lin Lin, “Disentanglement via entanglement: A unified method for Wannier localization,” *Multi-scale Modeling & Simulation* **16**, 1392–1410 (2018).
- ⁴² Kenneth Gotlieb, Zhenglu Li, Chiu-Yun Lin, Chris Jozwiak, Ji Hoon Ryoo, Cheol-Hwan Park, Zahid Hussain, Steven G. Louie, and Alessandra Lanzara, “Symmetry rules shaping spin-orbital textures in surface states,” *Phys. Rev. B* **95**, 245142 (2017).
- ⁴³ Dominik Gresch, QuanSheng Wu, Georg W. Winkler, Rico Häuselmann, Matthias Troyer, and Alexey A. Soluyanov, “Automated construction of symmetrized Wannier-like tight-binding models from ab initio calculations,” *Phys. Rev. Mater.* **2**, 103805 (2018).